SCIENCE&MILITARY

SCIENCE&MILITARY

The rationale for publishing this periodical by the Armed Forces Academy of General Milan Rastislav Štefánik is to enable the authors to publish their articles focused on particular scientific issues in the following areas: Military science, Natural Sciences, Engineering and Technology. Original scientific articles will be published twice a year.

Editorial Board

Address of the editorial office

SCIENCE & MILITARY

Dear Readers,

you have just opened the last issue of the Science & Military journal published in 2023. As the end of the year is approaching, it is time to evaluate what we have achieved in the past 12 months.

Throughout the year, we have tried to bring you the latest insights and findings from various fields of military science and provide you with inspiring articles that would contribute to broadening your knowledge. We are aware of the fact that publishing the results of scientific research plays an essential role in scientific work. It can be even said that it is a key aspect that determines the future of science. Science itself is becoming a living and dynamic organism, so if we want to contribute to the development of knowledge and make progress, we have to share our research results with others. Every paper in the Science & Military journal, including the articles written by young experts and doctoral students, is a piece of stone in the scientific mosaic. We acknowledge that supporting PhD students and enabling them to present the results of their research is an integral part of scientific work.

The primary goal of the editorial team this year was again to ensure that each issue of the Science & Military journal would consist of articles that meet the highest scientific standards. We carefully review all articles and make sure that they contain relevant and verifiable results. We believe that this guarantees a high level of their contents and their significant contribution to professional and scientific community. We take pride in the fact that Science & Military is an open-access journal, which ensures the wide dissemination of scientific research findings. Publishing scientific research results is of considerable significance for the progress of science and society as such. We have no doubt that the Science & Military journal contributes to achieving this goal and that it serves as a platform for authors of scientific papers.

Dear readers, let me briefly introduce the contents of the current issue.

The first among the peer-reviewed articles in this issue is the article titled „**Analysis of State-of-the-Art Software Solutions for Unstructured Outdoor Environment Perception in Goal-Oriented Navigation of Off-Road Unmanned Ground Vehicles**" written by Matej Vargovčík, Peter Pászto, Marian Kľúčik, Martin Smoľák, Patrik Štefka and Jakub Lenner. This paper deals with a comprehensive analysis of state-of-the-art software solutions designed for the perception of unstructured

outdoor environments, with a focus on their applicability in goal-oriented navigation for off-road unmanned ground vehicles (UGVs). The analysis suggests a phased approach for the development of autonomous navigation, where the initial phase relies on complex SLAM and teleoperation assistance, and the subsequent phase introduces an autonomous mode utilizing semantical terrain representation.

The following article written by Mikuláš Šostronek, Miroslav Matejček and Zdeno Baráni titled „**Design and Implementation of Output Circuitry for Millimetre-Wave Direct Detection Radiometer**". This paper presents a design and an implementation of an output circuitry for a millimetre-wave direct detection radiometer. This circuitry is based on commercially available ultra-low-noise op-amp and consists of an active anti-aliasing filter and DC amplifier. The prototype of this circuitry has been realized and evaluated.

The series of articles is closed with the paper titled „**Zoom Optical System for Thermal Camera in Optical Range 8-14 μm**" written by Chi Toan Dang, Vratislav Kreheľ and Michal Mozoľa. This article deals with the continuous infrared zoom systems with image quality and image stabilization maintained throughout the workflow, which are increasingly being used. A long wave infrared continuous zoom optical system with a 6x zoom ratio operating with an uncooled detector was designed.

Dear readers, let me thank you for your interest in our journal. I wish you a merry Christmas and a happy new year 2024, full of successes in your personal and professional life.

Brig. Gen. (ret.) Assoc. Prof. Eng. Boris ĎURKECH, CSc.
Chairman of the Editorial Board

Reviewers

ANALYSIS OF STATE-OF-THE-ART SOFTWARE SOLUTIONS FOR UNSTRUCTURED OUTDOOR ENVIRONMENT PERCEPTION IN GOAL-ORIENTED NAVIGATION OF OFF-ROAD UNMANNED GROUND VEHICLES

Matej VARGOVČÍK, Peter PÁSZTÓ, Marian KĽÚČIK, Martin SMOĽÁK, Patrik ŠTEFKA, Jakub LENNER

Abstract: This paper presents a comprehensive analysis of state-of-the-art software solutions designed for the perception of unstructured outdoor environments, with a focus on their applicability in goal-oriented navigation for off-road unmanned ground vehicles (UGVs). The analysis encompasses the evaluation of various sensors for UGV navigation, comparison of methods for extracting perceptual information from sensor data, and the development of a perception system based on the findings. The proposed system leverages advancements in simultaneous localization and mapping (SLAM), visual odometry, and traversability segmentation using 3D LiDAR and visual systems. The analysis suggests a phased approach for the development of autonomous navigation, where the initial phase relies on complex SLAM and teleoperation assistance, and the subsequent phase introduces an autonomous mode utilizing semantical terrain representation.

Keywords: UGV; Perception; Autonomous; Navigation; SLAM; Off-road.

1 INTRODUCTION

In this study, we explore the possibilities of extending navigation algorithms currently employed and under development by our company, RoboTech Vision, to adapt them for off-road environments. The unique challenges presented in these environments, characterized by a lack of regular structures and clearly distinguishable roads, necessitate a comprehensive analysis.

Given the abundance of state-of-the-art perception systems available in technical science, it is required to delineate the types of perceptual information crucial for successful navigation towards specified goals and to specify input data from which the information will be extracted. Section 2 defines the terrains that the UGVs will operate on and the sensors suitable for navigating these terrains.

Section 3 compares various existing methods for extracting relevant information from sensor data, evaluating their effectiveness in off-road environments. The methods are selected based on their relevance for the particular tasks and environments and their ranking in appropriate benchmarks addressing similar environments and use-cases.

Finally, Section 4 outlines a perception system based on this analysis and its integration into a complex traversability map creation and navigation system.

2 SITUATION

2.1 Environment

The target environment for UGV operation is the territory of Slovakia, and the analysis will be thus conducted on datasets from forest and field terrain (Figure 1). The primary objective of autonomous motion is to navigate through unpaved roads and paths, taking into account potential challenges such as partial erosion or coverage by vegetation and leaves. It's important to note that the analysis excludes extreme situations, such as motion on rocks, in brushwoods, or in swamps. Additionally, we assume a simplified scenario without the presence of snow and extreme weather conditions.
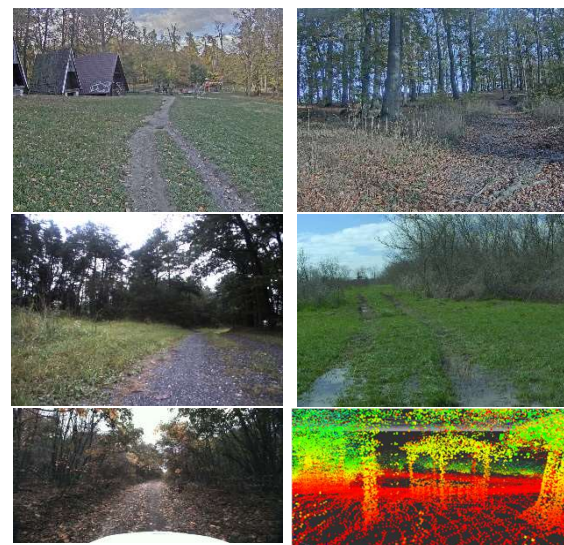

Fig. 1 Expected environment - camera images, bottom-right: LiDAR point-cloud
Source: author, datasets RUGD [1], RELLIS-3D [2], and Yamaha-seg [3].

2.2 Sensors

For navigation, UGV can use the following sensoric equipment:

- Odometry from incremental sensors in UGV chassis;
- IMU – accelerometer, gyroscope;

- Visual systems – RGB/IR cameras, depth cameras (TOF cameras, structured light cameras, stereo cameras);
- 3D LiDARs, in fog or smoke conditions extendible by MPR radars [4];
- Global satellite-based systems receivers (GPS, Glonass, Galileo).

Whereby two possible operation modes will be considered:

- Mode with full sensoric employment - appropriate for fast and reliable transfer;
- STEALTH mode - with employment of passive sensors only (no LiDARs, TOF cameras, and structured light cameras).

For the purpose of this work, we recorded a dataset with our RTV Crawler mobile robotic platform, equipped with locomotive odometry sensors (ams-OSRAM), IMU (Microstrain), a monocular front camera (Axis), a stereoscopic camera (Intel Realsense), a 16-channel 3D LiDAR (Velodyne), and a Glonass/GPS Receiver (NovAtel). The creation of this dataset aimed to include sensors of interest missing from RUGD [1] and Yamaha-seg [3] datasets or environments of interest missing from RELLIS-3D [2] dataset. Additionally, it allowed testing existing methods against new samples on which these methods were not originally developed. The sensor setup and dataset environments are illustrated in Figure 2.

Fig. 2 RTV Crawler mobile platform with sensoric setup in different environments during recording of our dataset
Source: author.

3 ANALYSIS OF PERCEPTION SYSTEM TASKS

Based on the sensors used and environmental conditions, we selected tasks to be performed by the perception system. The tasks will be described in the following sections, along with selected solutions, which will be tested on various datasets.

3.1 Simultaneous Localization and Mapping (SLAM) Using LiDAR

Localization is one of the basic requirements of autonomous UGVs, as information about the goal position relative to the UGV is essential during motion planning and execution. Additionally, localization is crucial for completing current UGV surroundings, which cannot be fully sensed from the current UGV pose, using a map created from previous poses.

Mapping involves storing sensor data (or processed information) in different poses of the UGV, which are mutually localized against each other. I.e. the essential and most complex element of mapping is correct and accurate localization. Therefore, in practice, mapping and localization are connected into one system - SLAM. When needed, mapping can be excluded, and localization is performed on a previously prepared static map.

Localization comprises two perceptional tasks: localization odometry and loop closure, which are combined using a pose graph.

3.1.1 Localization Odometry Using a 3D LiDAR

In contrast with odometry from incremental sensors in the UGV chassis (locomotive odometry), where motional information is retrieved from motor revolutions in a straightforward manner, localization odometry compares the sensorical description of the environment between consecutive poses of the UGV. UGV displacement is computed based on the relative motion of objects against the UGV. This type of odometry is resistant to skids and is usually significantly more accurate than locomotive odometry. Additionally, multiple types of odometry (LiDAR, visual, locomotive) can be combined to robustify the overall system, making it resistant to errors of individual odometries.

In the case of 3D LiDAR data (point-clouds), we used NDT registration [5] for pairing consecutive point-clouds. This registration, designed to match similar point-clouds, is suitable for the purpose of odometry due to its speed. It is designed to match similar point-clouds only, but despite this limitation, it is sufficient since similar consecutive captures are compared in the case of LiDAR odometry. Result of NDT odometry is illustrated in Figure 3.
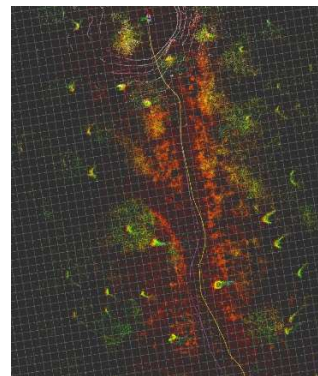
Fig. 3 NDT LiDAR odometry (yellow) compared to ground-truth UGV trajectory (purple) – locally it is highly accurate and consistent, although (like in the case of any odometry) its deviation increases gradually
Source: author.

3.1.2 Loop Closure

Due to the gradually increasing deviation of odometry, it is important to recognize previously mapped sites, when visited again, to interconnect the map. Site descriptors have been developed in computer science to optimize recognition and make it realizable in real-time.

In the analysis, we tested the applicability of ScanContext [6, 7] descriptor in off-road terrain, which proved suitable for such environment (Figure 4). For refining the mutual transformation between the recognized site and the actual pose, we used the GICP [8] registration algorithm, which is slower but more robust than NDT [5] registration used for LiDAR odometry (Figure 5).
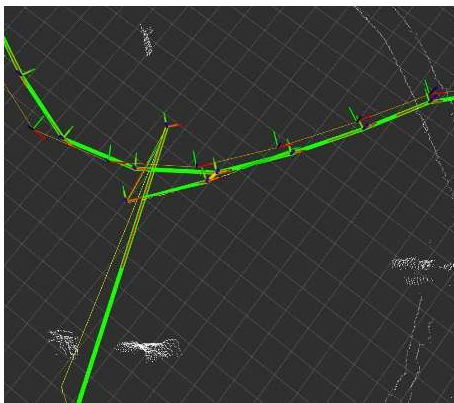
Fig. 4 A successful loop-closure marked by a short thick orange line between two nodes of a pose graph
Source: author.
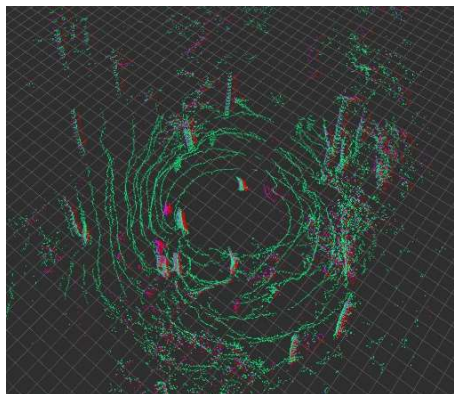
Fig. 5 Refining of the resulting transformation using GICP - current point-cloud transformed according to ScanContext recognition (red), point-cloud of the recognized site (green), point-cloud after transformation refinement (purple)
Source: author.

Final map shape is maintained by a pose graph [9], which uses odometry, loop-closure, GPS, and IMU measurements as input (Figure 6). Figure 7 depicts a final localization map created by placing LiDAR measurements on particular poses of the graph.
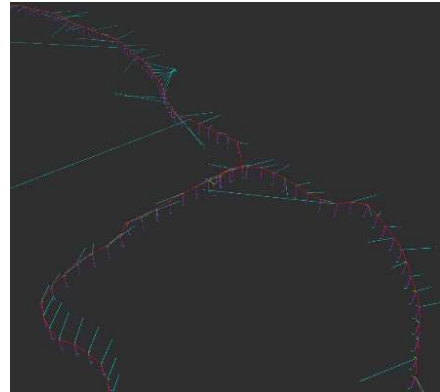
Fig. 6 Pose graph with odometry (red), loop-closure (orange), GPS (cyan), and IMU (purple) measurements
Source: author.
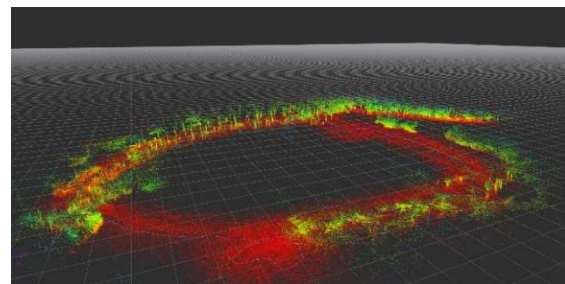
Fig. 7 Resulting localization map
Source: author.

In case that during development ScanContext appears as insufficient, it is additionally possible to use a machine-learning based method CVTNet [10], which shows significantly higher efficiency in benchmarks (although presumably requires higher maintenance due to requirement of dataset labeling and training).

3.2 Traversability Segmentation Using 3D LiDAR

The off-road environment includes a high amount of formations consisting of soft vegetation (e.g., grass clusters), which can appear as obstacles from a trivial view at point-cloud data, although they are actually traversable. For distinguishing such formations from real obstacles, it is appropriate to use modern neural-network methods with intuition-like attributes. We tested the operability of point-cloud neural networks against our datasets. DeepLabv3 ResNet101 [11] trained on TraversabilityClouds [12, 13] dataset proved successful (Figure 8). Good results were achieved also by SalsaNext [14] model trained on RELLIS-3D [2] dataset. However, it was observed that although the network had been trained for detailed classification (trees, soft vegetation, ground, puddle, human), in a different environment, it was able to correctly distinguish only two classes - trees and everything else (Figure 9).
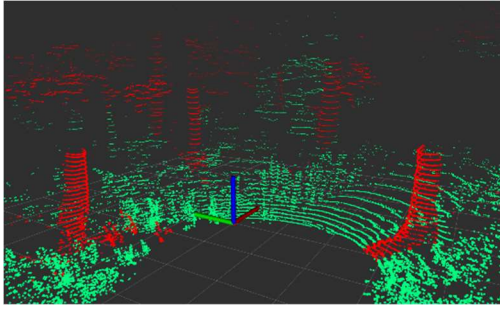
Fig. 8 Traversability estimation of a point-cloud using
DeepLabv3 ResNet101/TraversabilityClouds
Source: author.
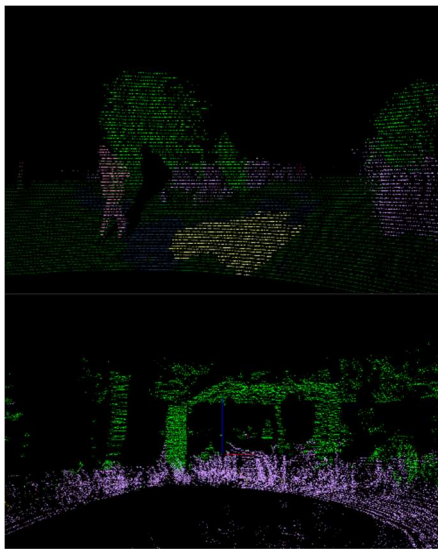
Fig. 9 SalsaNext - top: detailed segmentation in a familiar
environment of RELLIS-3D dataset; bottom:
segmentation of our data
Source: author.

3.3 Depth Estimation from Stereo-Pair of Images

In STEALTH mode, when active sensors measuring distances of points in the environment cannot be used, it is required to estimate the third dimension directly from camera images to project detected obstacles and terrain elements onto the traversability map. Depth estimation from a stereo-pair of images is a problem that has been targeted by computer vision science for a long time, resulting in a large number of different approaches, from traditional methods to modern ones with the use of machine learning.

Since a wider baseline between cameras of the stereoscopic system had proven as more appropriate for a complete comparable overview of depth estimation methods in off-road environments, we decided to prefer Nerian stereo camera data samples [15] and RELLIS-3D [2] dataset over our recorded dataset for this particular case.

From Figure 10, it is evident that strong randomly structured textures can induce minor problems for traditional methods that use mathematically defined similarity between

elements of the left and right camera image, but these problems can be eliminated in postprocessing by despeckling resulting images. Methods with neural networks offer, thanks to their intuition-like attributes, higher consistency of output, although their results differ in quality as well.
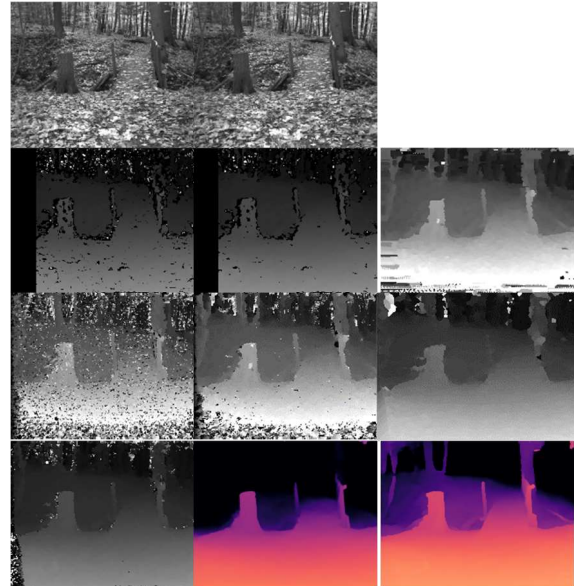
Fig. 10 Depth estimation. First row (left-to-right): left
camera image, right camera image [15]; Second row:
depth estimated by BM [16], SGBM [17], ASW [18]
algorithms; Third row: AD-Census V1 [19], SAD [20],
ZNCC [21]; Fourth row: SGM [22], ACVNet [23] trained
on Sceneflow [24] dataset, HITNet [25] trained
on Middlebury [26, 27, 28, 29, 30] dataset
Source: [15] (input data), author (processing).
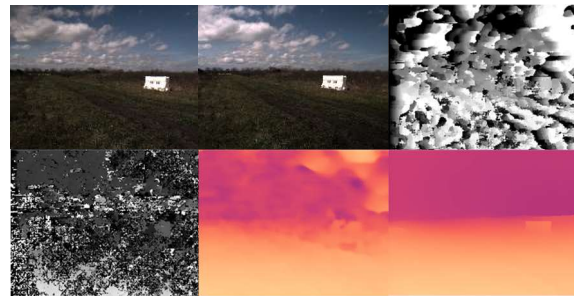
Fig. 11 Depth estimation from an uncalibrated stereo-pair
of images. First row (left-to-right): left camera image,
right camera image [2], depth estimated by ASW
algorithm; Second row: SGM, ACVNet trained
on KITTI [31, 32] dataset, HITNet trained
on Middlebury dataset
Source: [2] (input data), author (processing).

To verify robustness of algorithms against calibration errors (which can occur e.g. due to thermal expansion) we tested the methods on poorly calibrated images as well (Figure 11). Among the analyzed methods, the only successful one was HITNet [25], which was able to eliminate the sky, deal with grass texture, and correctly differentiate objects in front of the cameras. Despite the compactness of the results, it is suggested

to automatically recalibrate cameras [33] during the operation of the UGV. This ensures that the depth data accurately describe the spatial representation of the environment.

3.4 SLAM Using Visual Systém

The addition of visual SLAM into the perception system is desirable for two reasons:

- In STEALTH mode, UGV cannot take advantage of LiDARs; therefore, the use of LiDAR SLAM (Section 3.1) is not possible.
- Point-cloud data do not provide enough information value in a structurally monotonous environment to sustain fully operational localization (Figure 12).
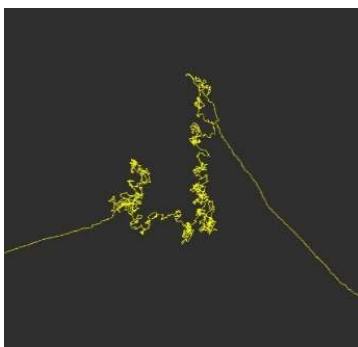
Fig. 12 Failure of LiDAR odometry in the middle of a grass field
Source: author.

3.4.1 Visual Odometry

In the analysis, we tested a basic odometry from RTAB-Map [34] system, using a stereo pair of cameras. The odometry uses BM [16] or SGBM [17] for depth estimation of camera pixels, which was sufficient for successful SLAM in an urban environment, however, did not prove as usable in off-road (Figure 13). The operability of this odometry can be improved using a more consistent depth estimation system (see Section 3.3).
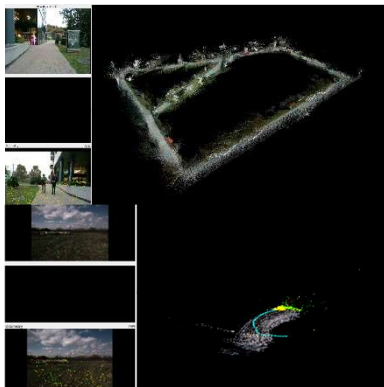
Fig. 13 SLAM using RTAB-Map [30] basic odometry - top: success in urban environment, bottom: failure in grass field in Rellis-3D [2]
Source: author.

Another option is to use OpenVINS [35] visual odometry system (also supported by RTAB-Map), which uses one or more cameras as input and additionally uses IMU data for a complex fusion. It was approved by us (Figure 14) and also in tests provided by authors of ROOAD [36] off-road dataset.
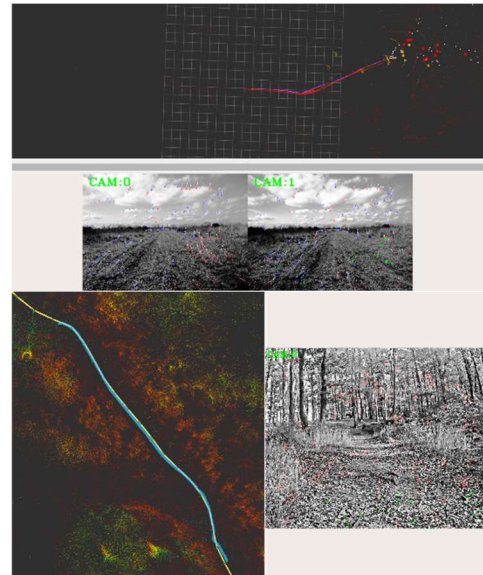
Fig. 14 Visual odometry using OpenVINS [35] - top: on Rellis-3D [2] dataset (red - ground-truth trajectory, purple - OpenVINS odometry); bottom: on our dataset (yellow - ground-truth trajectory, cyan - OpenVINS odometry)
Source: author.

3.4.2 Loop Closure Using Visual System

RTAB-Map offers a robust algorithm for loop closing [37], verified in urban environment by us (Figure 13) and in an off-road environment by the authors of the system (Figure 15).
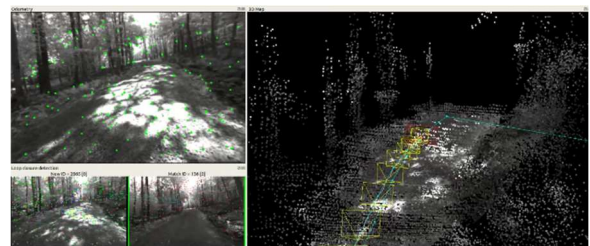
Fig. 15 Detection of a previously visited site and loop closure using RTAB-Map
Source: [38].

3.5 Traversability Segmentation Using Visual Systém

Semantic image segmentation is a common problem in computer vision science, and since it is a task requiring a certain degree of intuition, the best results are achieved by neural network models. In the analysis, we compared multiple models trained on different datasets with the purpose of segmentation in the off-road environment.
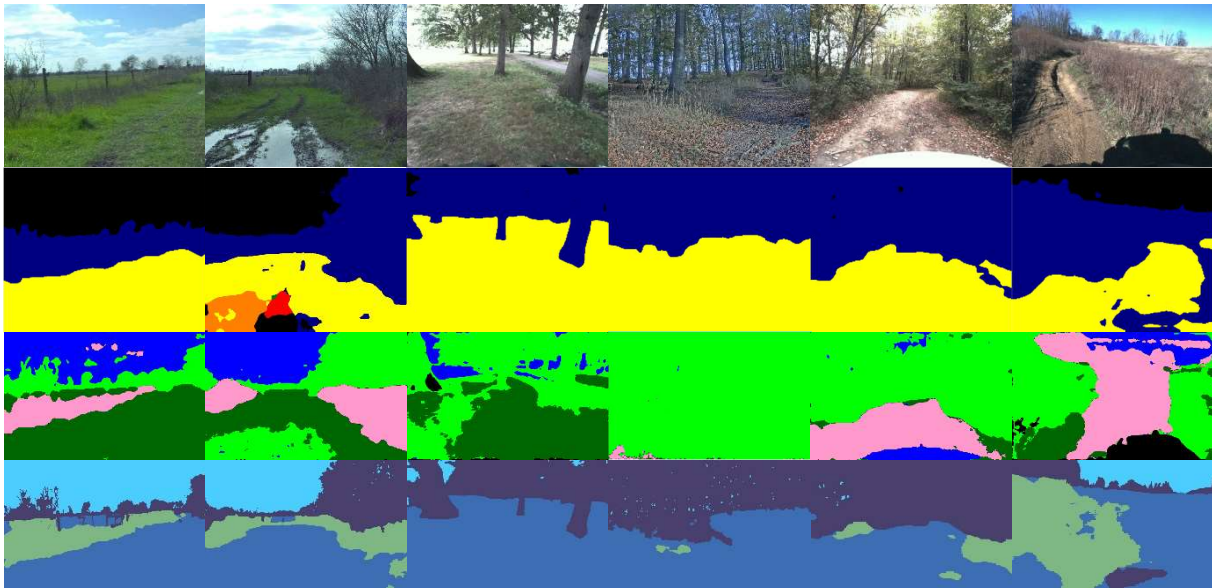
Fig. 16 Traversability segmentation of an image. First row: segmented images (from RELLIS-3D [2], Yamaha-seg [3], and our dataset). Second row: segmentation using GANav [39] model trained on RUGD [1] dataset. Third row: Unet [40] model trained within Traversability estimation [12, 13] project on RELLIS-3D [2] dataset. Fourth row: BiSeNet [41] model trained within OFFSEG [42] project on RUGD [1] dataset
Source: [2] (input data), [3] (input data), author (input data, processing).

From Figure 16, it is evident that off-road terrain segmentation is a difficult task even for state-of-the-art neural network models. The most successful are GANav [39] and OFFSEG [42] projects, whereby GANav shows slightly higher robustness (see the second image from the right), on the other hand, OFFSEG has higher sensitivity for detail. Both models were trained on RUGD [1] dataset, which proves to be more convenient for model training than RELLIS-3D [2] dataset because it is richer regarding environmental variety. Also, Yamaha-seg [3] dataset appears as a promising ground for model training due to the variety of field path images contained (see the failure of all networks on the rightmost image, which could be eliminated by further training on this dataset).

4 OUTLINE OF A COMPLEX PERCEPTION SYSTEM

Based on the performed analysis, we suggest splitting the development of autonomous navigation into two phases.

In the first phase, UGV will use complex SLAM from combined sensorical data (Section 3.1, Section 3.4), which is currently supported by operational and reliable systems. Since traversability segmentation of terrain, although promising and successful to a high degree, still brings risks and needs more development, in this phase, it will be used only for marginal tasks of refining a detailed trajectory during UGV motion. This refinement will be additionally enhanced by terrain roughness analysis systems, which are more straightforward (not included in the analysis since our company already has working solutions for that). During path planning,

which requires more responsibility, the teleoperator will be asked for outlining an approximate path that will be preferentially followed by UGV. This lower level of autonomy can introduce multiple advantages:

- Attention is demanded only when asking for a next goal. This way, the teleoperator can concentrate on other tasks or operate multiple UGVs at once.
- During navigation, UGV is not dependent on reliable uninterrupted high bandwidth communication, since communication is required only occasionally, ideally in safe locations, where UGV can afford waiting for next instructions.
- In STEALTH mode transmission at the UGV side is reduced to a short broadcast of data about the situation around the new position, from the operator side it is required to transmit only information about the new goal and approximate path outline.
- Navigation in a familiar area (e.g., mapped terrain with a path marked in advance, return motion along the same path, repeated operation with identical paths as in previous operations) can be fully autonomous, since the UGV can follow known paths.

The second phase will introduce an autonomous mode, allowing the UGV to reach specified goals independently of the operator, even in an unfamiliar area, whereby semantic terrain representation will be used in a complete manner, tuned, and trained for general operation in the off-road environment.

Outline of such perception system, whose development is divided into two phases, is illustrated in Figure 17.
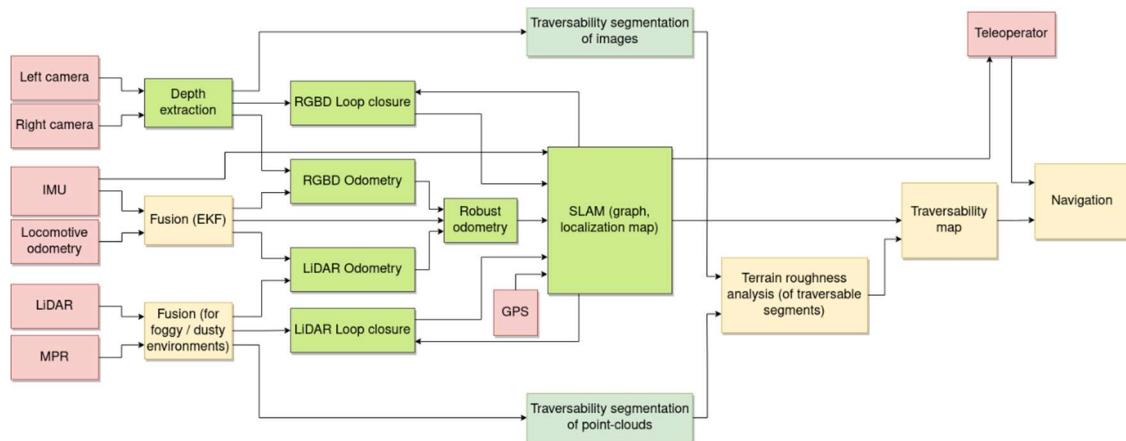
Fig. 17 Outline of the perception system and its application onto UGV navigation; red - inputs, green - perception system components analyzed in this work (pale green - second phase), yellow - other components of navigation system
Source: author.

.
5 CONCLUSION

This paper has presented a comprehensive overview of various perception tasks essential for resolving navigation challenges, alongside state-of-the-art methods tailored for off-road navigation. The selected solutions were tested against diverse environmental samples, extending beyond their original presentation by their authors, and included solutions primarily designed for different environments (urban, indoor) to assess their applicability in off-road settings.

The successful operation of a subset of the chosen methods for each predefined task across most tested environmental samples underscores the maturity of the current state of artificial intelligence in scientific research for deployment in autonomous or semi-autonomous off-road navigation. The paper has highlighted the advantages of such navigation over commonly used pure teleoperational methods for guiding robots in unexplored or partially unknown environments. Additionally, the paper outlined the concept of a navigation system with integrated perception components for the specified tasks.

However, off-road perception remains a relatively marginal focus in the scientific field. Despite the development of pioneering algorithms explicitly designed for this purpose and the collection of initial off-road datasets, this area lacks a high-quality platform providing multi-sensorial data for development, along with a standardized methodology for the assessment and comparison of off-road perception methods. The absence of such a platform, comparable to the KITTI [31] dataset for urban environments, hinders the development and selection of solutions that are not only operationally feasible but also most suitable for specific off-road navigation challenges. Therefore, future research, particularly before the second phase of development, should prioritize the creation of a methodological core and data collection for such a platform.

References

[1] WIGNESS, Maggie, EUM, Sungmin, ROGERS, John G, HAN, David and KWON, Heesung. A RUGD Dataset for Autonomous Navigation and Visual Perception in Unstructured Outdoor Environments. In *International Conference on Intelligent Robots and Systems (IROS)*. 2019. Available at: https://doi.org/10.1109/IROS40897.2019.8968283.

[2] JIANG, Peng, OSTEEN, Philip R., WIGNESS, Maggie B. and SARIPALLI, Srikanth. RELLIS-3D Dataset: Data, Benchmarks and Analysis. In *2021 IEEE International Conference on Robotics and Automation (ICRA)*. Online. 2020. P. 1110–1116. Available at: https://doi.org/10.1109/ICRA48506.2021.9561251.

[3] MATURANA, Daniel, CHOU, Po-wei, UENOYAMA, Masashi and SCHERER, Sebastian A. Real-Time Semantic Mapping for Autonomous Off-Road Navigation. In *International Symposium on Field and Service Robotics*. Online. 2017. Available at: https://doi.org/10.1007/978-3-319-67361-5_22.

[4] FRITSCHE, Paul, KUEPPERS, Simon, BRIESE, Gunnar and WAGNER, Bernardo. Radar and LiDAR Sensorfusion

in Low Visibility Environments. In *International Conference on Informatics in Control, Automation and Robotics*. Online. 2016. Available at: https://api.semanticscholar.org/CorpusID:42431 812.

[5] BIBER, P. and STRASSER, W. The normal distributions transform: a new approach to laser scan matching. In *Proceedings 2003 IEEE/RSJ International Conference on Intelligent Robots and Systems (IROS 2003) (Cat. No.03CH37453)*. 2003. p. 2743–2748. Available at: https://doi.org/10.1109/IROS.2003.1249285.

[6] KIM, Giseop, CHOI, Sunwook and KIM, Ayoung. Scan Context++: Structural Place Recognition Robust to Rotation and Lateral Variations in Urban Environments. *IEEE Transactions on Robotics*. 2021. Available at: https://doi.org/10.1109/TRO.2021.3116424.

[7] KIM, Giseop and KIM, Ayoung. Scan Context: Egocentric Spatial Descriptor for Place Recognition within 3D Point Cloud Map. In *Proceedings of the IEEE/RSJ International Conference on Intelligent Robots and Systems*. October 2018. Available at: https://doi.org/ 10.1109/IROS.2018.8593953.

[8] KOIDE, Kenji, YOKOZUKA, Masashi, OISHI, Shuji and BANNO, Atsuhiko. *Voxelized GICP for Fast and Accurate 3D Point Cloud Registration*. 2020. EasyChair Preprint no. 2703. Available at: https://doi.org/10.1109/ICRA48506.2021.9560 835.

[9] KÜMMERLE, Rainer, GRISETTI, Giorgio, STRASDAT, Hauke, KONOLIGE, Kurt and BURGARD, Wolfram. G2o: A general framework for graph optimization. In *2011 IEEE International Conference on Robotics and Automation*. 2011. p. 3607–3613. Available at: https://doi.org/10.1109/ICRA.2011.5979949.

[10] MA, Junyi, XIONG, Guangming, XU, Jingyi and CHEN, Xieyuanli. CVTNet: A Cross-View Transformer Network for LiDAR-Based Place Recognition in Autonomous Driving Environments. *IEEE Transactions on Industrial Informatics*. 2023. Available at: https://doi.org/10.1109/TII.2023.3313635.

[11] CHEN, Liang-Chieh, PAPANDREOU, George, SCHROFF, Florian and ADAM, Hartwig. Rethinking Atrous Convolution for Semantic Image Segmentation. *CoRR*. Online. 2017. Available at: http://arxiv.org/abs/1706.05587.

[12] AGISHEV, Ruslan, PETŘÍČEK, Tomáš and ZIMMERMANN, Karel. Trajectory Optimization Using Learned Robot-Terrain Interaction Model in Exploration of Large Subterranean Environments. In *IEEE Robotics and Automation Letters*. 2022. Vol. 7, no. 2p.

3365–3371. Available at: https://doi.org/ 10.1109/LRA. 2022.3147332.

[13] AGISHEV, Ruslan, ZIMMERMANN, Karel, PECKA, Martin and SVOBODA, Tomáš. MonoForce: Self-supervised learning of physics-aware grey-box model for predicting the robot-terrain interaction. *arXiv preprint arXiv*:2309.09007. 2023.

[14] CORTINHAL, Tiago, TZELEPIS, George and AKSOY, Eren Erdal. *SalsaNext: Fast, Uncertainty-aware Semantic Segmentation of LiDAR Point Clouds for Autonomous Driving*. 2020. Available at: https://doi.org/10.1007/ 978-3-030-64559-5_16.

[15] Automatic Camera Re-Calibration for Robust Stereo Vision. Online. 2023. [Accessed 24 November 2023]. Available at: https://www.youtube.com/watch?v=2QGnOwf QKYo.

[16] GRAMMALIDIS, Nikos and STRINTZIS, Michael. G. Disparity and occlusion estimation in multiocular systems and their coding for the communication of multiview image sequences. In *IEEE Transactions on Circuits and Systems for Video Technology*. 1998. Vol. 8, no. 3p. 328–344.

[17] HIRSCHMULLER, Heiko. Stereo Processing by Semiglobal Matching and Mutual Information. In *IEEE Transactions on Pattern Analysis and Machine Intelligence*. 2008. Vol. 30, no. 2p. 328–341. Available at: https://doi.org/10.1109/TPAMI.2007.1166.

[18] YOON, Kuk-Jin and KWEON, In So. Adaptive support-weight approach for correspondence search. In *IEEE Transactions on Pattern Analysis and Machine Intelligence*. 2006. Vol. 28, no. 4p. 650–656. Available at: https://doi.org/10.1109/TPAMI.2006.70.

[19] MEI, Xing, SUN, Xun, ZHOU, Mingcai, JIAO, Shaohui, WANG, Haitao and ZHANG, Xiaopeng. On building an accurate stereo matching system on graphics hardware. In *2011 IEEE International Conference on Computer Vision Workshops (ICCV Workshops)*. 2011. p. 467–474. Available at: https://doi.org/10.1109/ICCVW.2011.6130280.

[20] HAMZAH, Rostam Affendi, RAHIM, Rosman Abd and NOH, Zarina Mohd. Sum of Absolute Differences algorithm in stereo correspondence problem for stereo matching in computer vision application. In *2010 3rd International Conference on Computer Science and Information Technology*. 2010. p. 652–657. Available at: https://doi.org/10.1109/ICCSIT.2010.5565062.

[21] CHANG, Qiong, ZHA, Aolong, WANG, Weimin, LIU, Xin, ONISHI, Masaki, LEI, Lei, ER, Meng Joo and MARUYAMA, Tsutomu. *Efficient stereo matching on embedded GPUs*

with zero-means cross correlation. 2022. Available at: https://doi.org/10.1016/j.sysarc. 2021.102366

[22] HERNANDEZ-JUAREZ, D., CHACÓN, A., ESPINOSA, A., VÁZQUEZ, D., MOURE, J.C. and LÓPEZ, A.M. Embedded Real-time Stereo Estimation via Semi-global Matching on the GPU. In *Procedia Computer Science*. Online. 2016. Vol. 80, p. 143–153. Available at: https://doi.org/10.1016/j.procs.2016.05.305.

[23] XU, Gangwei, CHENG, Junda, GUO, Peng and YANG, Xin. *Attention Concatenation Volume for Accurate and Efficient Stereo Matching*. 2022. Available at: https://doi.org/10.1109/CVPR52688.2022.0126 4 .

[24] MAYER, N., ILG, E., HÄUSSER, P., FISCHER, P., CREMERS, D., DOSOVITSKIY, A. and BROX, T. A Large Dataset to Train Convolutional Networks for Disparity, Optical Flow, and Scene Flow Estimation. In *IEEE International Conference on Computer Vision and Pattern Recognition (CVPR)*. Online. 2016. Available at: https://doi.org/10.1109/CVPR.2016.438

[25] TANKOVICH, Vladimir, HÄNE, Christian, ZHANG, Yinda, KOWDLE, Adarsh, FANELLO, Sean and BOUAZIZ, Sofien. *HITNet: Hierarchical Iterative Tile Refinement Network for Real-time Stereo Matching*. 2023.

[26] SCHARSTEIN, D., SZELISKI, R. and ZABIH, R. A taxonomy and evaluation of dense two-frame stereo correspondence algorithms. In *Proceedings IEEE Workshop on Stereo and Multi-Baseline Vision (SMBV 2001)*. 2001. p. 131–140. Available at:

https://doi.org/10.1109/SMBV.2001.98877.

[27] SCHARSTEIN, D. and SZELISKI, R. High-accuracy stereo depth maps using structured light. In *2003 IEEE Computer Society Conference on Computer Vision and Pattern Recognition, 2003. Proceedings*. 2003. p. I-I. Available at: https://doi.org/10.1109/CVPR.2003.1211354.

[28] SCHARSTEIN, Daniel and PAL, Chris. Learning Conditional Random Fields for Stereo. In *2007 IEEE Conference on Computer Vision and Pattern Recognition*. 2007. p. 1–8. Available at: https://doi.org/CVPR. 2007.383191.

[29] HIRSCHMULLER, Heiko and SCHARSTEIN, Daniel. Evaluation of Cost Functions for Stereo Matching. In *2007 IEEE Conference on Computer Vision and Pattern Recognition*. 2007. p. 1–8. Available at: https://doi.org/10.1109/CVPR.2007.383248 .

[30] SCHARSTEIN, Daniel, HIRSCHMÜLLER, Heiko, KITAJIMA, York, KRATHWOHL, Greg, NEŠIĆ, Nera, WANG, Xi and WESTLING, Porter. High-Resolution Stereo Datasets with Subpixel-Accurate Ground Truth. In JIANG, Xiaoyi, HORNEGGER, Joachim and KOCH, Reinhard (eds..), *Pattern Recognition*. Cham: Springer International Publishing, 2014. p. 31–42. ISBN 978-3-319-11752-2. Available at: https://doi.org/10.1007/978-3-319-11752-2_3.

[31] GEIGER, Andreas, LENZ, Philip and URTASUN, Raquel. Are we ready for Autonomous Driving? The KITTI Vision Benchmark Suite. In *Conference on Computer Vision and Pattern Recognition (CVPR)*. 2012. Available at: https://doi.org/10.1109/CVPR.2012.6248074.

[32] MENZE, Moritz and GEIGER, Andreas. Object Scene Flow for Autonomous Vehicles. In *Conference on Computer Vision and Pattern Recognition (CVPR)*. 2015. Available at: https://doi.org/10.1109/CVPR.2015.7298925.

[33] MARKO, Thomas and KUBINGER, Wilfried. Automatic Stereo Camera Calibration in Real-World Environments Without Defined Calibration Objects. In *Proceedings of the 29th DAAAM International Symposium*. 2018. p. 102–108. ISBN 9783902734204.

[34] LABBÉ, Mathieu and MICHAUD, François. Long-term online multi-session graph-based SPLAM with memory management. *Autonomous Robots*. Online. November 2017. Vol. 42, no. 6p. 1133. Available at: https://doi.org/10.1007/s10514-017-9682-5.

[35] GENEVA, Patrick, ECKENHOFF, Kevin, LEE, Woosik, YANG, Yulin and HUANG, Guoquan. OpenVINS: A Research Platform for Visual-Inertial Estimation. In *Proc. of the IEEE International Conference on Robotics and Automation*. 2020.

[36] CHUSTZ, George and SARIPALLI, Srikanth. *ROOAD: RELLIS Off-road Odometry Analysis Dataset*. 2021. Available at: https://doi.org/10.1109/IV51971.2022.9827133.

[37] LABBÉ, Mathieu and MICHAUD, François. Online global loop closure detection for large-scale multi-session graph-based SLAM. In *2014 IEEE/RSJ International Conference on Intelligent Robots and Systems*. 2014. p. 2661–2666. Available at: https://doi.org/10.1109/IROS.2014.6942926.

[38] RTAB-Map: Four Kilometers Walk in Forest (an uncut real-time visual SLAM demo). Online. 2023. [Accessed 24 November 2023]. Available at: https://www.youtube.com/watch?v=G-5jesjNfLc.

[39] GUAN, Tianrui, KOTHANDARAMAN, Divya, CHANDRA, Rohan, SATHYAMOORTHY, Adarsh Jagan, WEERAKOON, Kasun and MANOCHA, Dinesh. GA-Nav: Efficient Terrain Segmentation for Robot Navigation

in Unstructured Outdoor Environments. In *IEEE Robotics and Automation Letters*. 2022. Vol. 7, no. 3p. 8138–8145. Available at: https://doi.org/10.1109/LRA.2022.3187278.

[40] RONNEBERGER, Olaf, FISCHER, Philipp and BROX, Thomas. *U-Net: Convolutional Networks for Biomedical Image Segmentation*. 2015. Available at: https://doi.org/10.1007/ 978-3-319-24574-4_28.

[41] YU, Changqian, WANG, Jingbo, PENG, Chao, GAO, Changxin, YU, Gang and SANG, Nong. *BiSeNet: Bilateral Segmentation Network for Real-time Semantic Segmentation*. 2018. Available at: https://doi.org/10.1007/978-3-030-01261-8_20.

[42] VISWANATH, Kasi, SINGH, Kartikeya, JIANG, Peng, SUJIT, P. B. and SARIPALLI, Srikanth. OFFSEG: A Semantic Segmentation Framework For Off-Road Driving. In *2021 IEEE 17th International Conference on Automation Science and Engineering (CASE)*. 2021. p. 354–359. Available at: http://10.1109/CASE49439.2021.9551643.

Eng. Matej **VARGOVČÍK**
RoboTech Vision s.r.o.
Červený kameň 61
900 89 Častá
Slovak Republic
E-mail: vargovcik@robotechvision.com

Eng. Peter **PÁSZTÓ**, PhD.
RoboTech Vision s.r.o.
Červený kameň 61
900 89 Častá
Slovak Republic
E-mail: paszto@robotechvision.com

Eng. Marian **KĽÚČIK**
RoboTech Vision s.r.o.
Červený kameň 61
900 89 Častá
Slovak Republic
E-mail: klucik@robotechvision.com

Eng. Martin **SMOĽÁK**
RoboTech Vision s.r.o.
Červený kameň 61
900 89 Častá
Slovak Republic
E-mail: smolak@robotechvision.com

Eng. Patrik **ŠTEFKA**
RoboTech Vision s.r.o.
Červený kameň 61
900 89 Častá
Slovak Republic
E-mail: stefka@robotechvision.com

Eng. Jakub **LENNER**
RoboTech Vision s.r.o.
Červený kameň 61
900 89 Častá
Slovak Republic
E-mail: lenner@robotechvision.com

Matej VARGOVČÍK studied robotics on Faculty of Electrical Engineering and Information Technology of STU in Bratislava. During his studies he was developing number of significant scientific works. He implemented his knowledge in RoboTech Vision Ltd. company in which he is currently working. He is responsible for development of autonomous navigation an localization algorithms. He also actively collaborates with the scientific comunity in his field and is contributing his solutions on GitHub platform.

Peter PÁSZTÓ studied robotics on Faculty of Electrical Engineering and Information Technology of STU in Bratislava. He is one of the founders and CEOs of RoboTech Vision Ltd. Throughout his university studies he has focused on image processing algorithms and their application in the field of mobile robotics (navigation and localization). During PhD studies he was awarded together with his team (now already CEOs of company) at a scientific conference in Rijeka, Croatia for an image processing algorithm detecting obstacles in front of a mobile robot navigated only by a smartphone running on Android OS.

Marian KĽÚČIK studied robotics on Faculty of Electrical Engineering and Information Technology of STU in Bratislava. He is one of the founders and CEOs of RoboTech Vision Ltd. During his studies he focused on the development of a robot with a combined chassis. He was also working on development of genetic algorithms for navigation and localization of his robotic platform. His skills include programming in multiple programming languages, controlling various operating systems, control system development, mechanics, control software and electronics. He focuses on the development of communication layer software and the configuration of OS in his company.

Martin SMOĽÁK has been involved in mobile robotics since secondary school. He was also involved in telemedicine projects and developed smart cars for the police in the past. He studied robotics on Faculty of Electrical Engineering and Information Technology of STU in Bratislava. Within RoboTech Vision Ltd. (of which he is also on of founders and CEOs), he focuses mainly on the development of lower-level control software, hardware, mechanics, and navigation algorithms and mobile robotic platforms design.

Patrik ŠTEFKA studied robotics on Slovak University of Technology in Bratislava. Presently he is working in RoboTech Vision Ltd. company where he is responsible for development and integration of AI methods and neural network data processing into human interaction, navigation and localization algorithms.

Jakub LENNER studied robotics on Slovak University of Technology in Bratislava. Presently he is working in RoboTech Vision Ltd. company where he is cooperating on development of visual navigation and path-planning methods. He is also author of several scientific publications in the field of precise robot path-planning for docking algorithms using visual systems and image processing.

DESIGN AND IMPLEMENTATION OF OUTPUT CIRCUITRY
FOR MILLIMETER-WAVE DIRECT DETECTION RADIOMETER

Mikuláš ŠOSTRONEK, Miroslav MATEJČEK, Zdeno BARÁNI

Abstract: This paper presents a design and an implementation of an output circuitry for a millimeter-wave direct detection radiometer. This circuitry is based on commercially available ultra-low-noise op-amp and consist of an active anti-aliasing filter and DC amplifier. The prototype of this circuitry has been realized and evaluated.

Keywords: Millimeter-wave radiometer; Direct detection radiometer; Output radiometer circuitry; Anti-aliasing filter.

1 INTRODUCTION

Millimeter-wave (MMW) radiometers are very sensitive broadband receivers that operate at millimeter wavelengths. They can measure physical temperature or emissivity of objects.

Some of most important applications of MMW radiometry are [1]:

- Hidden weapon and contraband detection;
- Weapon guidance and missile seekers;
- Radio astronomy;
- Remote sensing of atmosphere;
- Remote measurement of temperature;
- Humidity and water vapor measurement from ground and space;
- Etc.

Because radiometers are passive receivers, their use for military purposes is very advantageous since their activity cannot be detected by any means.

MMW radiometers measure the received noise power at the antenna output with very small amplitudes at noise level. For this reason, the use of low-noise output circuits of the radiometer is crucial.

This article describes the construction of low-noise circuits, which are necessary for processing the noise signal from the output of the radiometer. These radiometer output circuits include an anti-aliasing filter and a DC amplifier. The purpose of these circuits is signal conditioning for the analog-to-digital converter (ADC).

2 RADIOMETER FRONT END PROPERTIES

As a radiometric front-end RF module, we used direct detection radiometric module from Farran Technology Ltd. as is shown in Fig. 1.
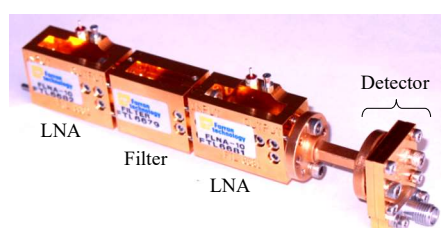
Fig. 1 Direct detection radiometric module
Source: [2].

The block scheme of the radiometric module connection is shown in Fig. 2.
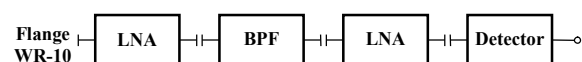
Fig. 2 The block scheme of the radiometric module
Source: author.

where LNA is Low Noise Amplifier, BPF is Band Pass Filter and Detector is diode detector.

The specification of the radiometric module is as follows [3]:

- Frequency: 93 to 96 GHz;
- Total gain: 50 dB (min.), 60 dB (typical);
- Noise figure: 4.5 dB maximum;
- Power supply: +5V DC;
- Filter bandwidth: min. 500 MHz.

These parameters are declared by the manufacturer, but the measured data (specifically the bandwidth of the band pass filter - BPF) are much better as is shown in Tab. 1.

Tab. 1 Radiometer RF frond-end parameters

Circuit	Type	NF [dB]	NF [-]	Gain [dB]
1. LNA	FTL 6681	2.903	1.95	27.348
2. LNA	FTL 6682	2.93	1.96	26.679
BPF	FTL 6679	0.9	1.23	-0.9
RF Front End	---	2.907	1.953	53.127

Source: [2].

The detection diode is a W-band planar detector without applied bias. It is a logarithmic-linear detector based on Schottky diode technology. Minimum sensitivity is approximately 2.2 V/mW. The detected voltage has a positive polarity.

3 THE LIMIT SIGNAL LEVELS AT THE RADIOMETER OUTPUT

When designing a DC (direct current) amplifier, it is necessary to calculate the limit values of the voltage that will be at the output of the radiometric module.

3.1 The maximum voltage value at the radiometer output

Consider the maximum dynamic range of the signal from the radiometer output will be if the temperature of the antenna is $T_A = 0$ K and the temperature of the reference load will be $T_R = 313$ K. The difference between the temperature of the reference load and the antenna will be $\Delta T_{MAX} = 313$ K. However, we also must include the system noise temperature, too. Temperature ΔT_{MAX} together with the noise temperature of the system T_N corresponds to the power of the radiometer output:

$$P_{MAX} = k_B(\Delta T_{MAX} + T_N)B =$$
$$= 1.38 \times 10^{-23} \cdot (313 + 276.254) \cdot 11.7 \times 10^9 =$$
$$= 95.141 \times 10^{-12} \text{ W.} \qquad (1)$$

After amplification by a radiometric module with a gain of $G = 53.127$ dB, we receive a signal at the input of the detector:

$$P_{max} = P_{MAX} G$$
$$P_{max} = 95.141 \times 10^{-12} \cdot 10^{\frac{53.127}{10}} =$$
$$= 19.5464 \times 10^{-6} = 19.5464 \text{ μW.} \qquad (2)$$

Since the sensitivity of the detector is 2.2 V/mW (2200 V/W) [3], then the amplitude of the signal behind the detector at the input of the DC amplifier will be:

$$U_{max} = 19.5464 \times 10^{-6} \cdot 2200 = 43 \text{ mV}_{pp}. \quad (3)$$

3.2 The minimum voltage value at the radiometer output

The minimum voltage at the radiometer output is reached if $T_A = 0$K. Then the power at the radiometer output will be:

$$P_{min} = k_B(0\text{K} + T_N)B =$$
$$= 1.38 \times 10^{-2} \cdot (0 + 276.254) \cdot 11.7 \times 10^9 =$$
$$= 44.604 \times 10^{-12}\text{W.} \qquad (4)$$

After amplification by the radiometric module, we get:

$$P_{min\,det} = P_{min}\,G =$$
$$= 44.604 \times 10^{-12} \cdot 10^{\frac{53.127}{10}-6} = \qquad (5)$$
$$= 9.163 \times 10^{-6} = 9.163 \text{ μW.}$$

At the output of the detector, we get:

$$U_{min} = 9.163 \times 10^{-6} \cdot 2200 = 20.1603 \text{ mV}_{pp}. \quad (6)$$

3.3 Voltage value at the output of the radiometer when measuring a 1K thermal difference

The minimum signal at the output of the radiometer, which should be processed without degradation, is e.g., 1K. This will be if the antenna temperature is for example $T_A = 312$ K and the temperature of the reference load is $T_{ref} = 313$ K. Thus, the minimum signal at the input of the DC amplifier for a resolution of 1K will be:

$$\Delta P_{1K} = k_B(1\text{K})B =$$
$$= 1.38 \times 10^{-2} \cdot (1) \cdot 11.7 \times 10^9 =$$
$$= 16.146 \times 10^{-14} \text{ W.} \qquad (7)$$

After amplification by the radiometric module, it will be:

$$\Delta P_{out\,1K} = \Delta P_{1K} 10^{\frac{G}{10}} = 16.146 \times 10^{-14} \cdot 10^{\frac{53.127}{10}}$$
$$= 33.556.10^{-9} = 33.556 \text{ nW.} \qquad (8)$$

At the detector output with a sensitivity of 2200 V/W we get

$$U_{1K} = 33.556 \times 10^{-9} \cdot 2200 = 73.8232 \times 10^{-6} =$$
$$= 73.8232 \text{ μV}_{pp}. \qquad (9)$$

The Fig. 3 serves to understand these calculations. From the above text the following conclusion can be drawn:

- For the brightness temperature $T_A = 0$ K, the voltage at the detector output will be approx. 20.1603 mV$_{pp}$.
- For the maximum brightness temperature $T_A = 313$ K, the voltage at the detector output will be approx. 43 mV$_{pp}$.
- A brightness temperature difference of 1 K will represent a voltage increase at the detector output of 73.8223 μV$_{pp}$.

4 DC AMPLIFIER DESIGN

When designing a DC amplifier, it is necessary to evaluate the influence of its own noises on the radiometer resolution.

4.1 Calculation of the influence of the inherent noise of the DC amplifier

When sampling the signal from the DC amplifier by the A/D converter (ADC), we will apply digital integration with the integration time $\tau = 10$ ms.

This integration time corresponds to a bandwidth of 50 Hz (more details well be explained in Paragraph 5).

As a DC amplifier, we will use an ultra-low-noise operational amplifier (OA) from Analog Devices AD8599. The OA has a spectral voltage noise density of 1.07 nV/$\sqrt{\text{Hz}}$ at a frequency of 1 Hz, and from a frequency of 10 Hz this noise increases to 1.5 nV/$\sqrt{\text{Hz}}$. The average value of the spectral voltage noise density is 1.285 nV/$\sqrt{\text{Hz}}$.
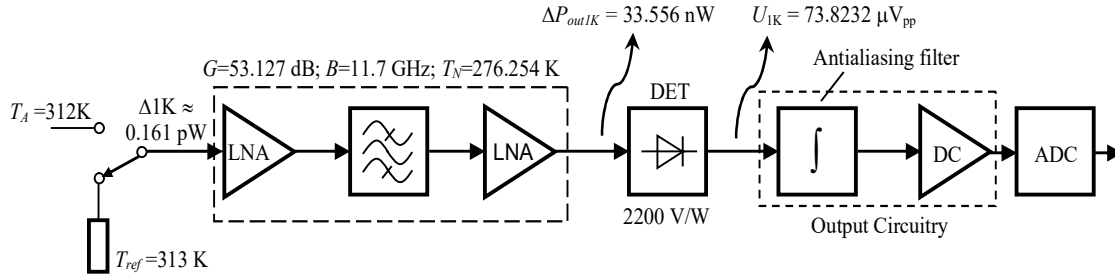
Fig. 3 Power and voltage values on the radiometric module of Farran Technology Ltd.
Source: author.

The noise signal of this OA in the band up to 50 Hz will be:

$$S_N = \sqrt{50} \cdot 1.285 \times 10^{-9} = 9.0863 \text{ nV.} \quad (10)$$

For the resolution of the brightness temperature 1K at the radiometer input, the output of radiometer will give a voltage difference of 43.66 μV. Compared to the used OA noise of 9.0863 nV so this noise will not have a significant effect on the resolution ability of the radiometer.

4.2 Calculation of the DC amplifier gain

Next step is to calculate how much gain should be set on the DC amplifier so that the maximum value reaches 95% of the range of the ADC (for example +/-5V = 10V).

The AD8599 allows to amplify signals with a voltage gain of 110 dB. If we consider that at the maximum voltage from the output of the radiometer is approx. 43 mV and we require 95% of 10 V at the OA output, then its gain should be:

$$G_{OA} = 0.95 \cdot 10/(43 \times 10^{-3}) = 220.9, \quad (11)$$

and by converting to decibels, we get a gain of 46.9 dB.

When measuring the minimum value at the input of the radiometer (for $T_A = 0$ K), we get a signal at the output of the DC amplifier:

$$S_{MIN} = 20.1603 \times 10^{-3} \cdot 220.9 = 4.4534 \text{ V,} \quad (12)$$

and when measuring the maximum value at the input of the radiometer (for $T_A = 313$ K) will be

$$S_{MAX} = 43 \times 10^{-3} \cdot 220{,}9 = 9.4 \text{ V.} \quad (13)$$

For a resolution of 1 K, it will be at the output of the amplifier:

$$\frac{S_{MAX} - S_{MIN}}{313} = \frac{9.4 - 4.4534}{312} = 15.854 \times 10^{-3} \approx 16 \text{ mV.} \quad (14)$$

Since the ADC has a dynamic range of ± 5 V, it is necessary to include a zero-level adjustment circuit before the DC amplifier. This circuit will set the minimum value of the radiometer output to a level

close to the lower limit of the range of the ADC (± 5V).

5 THE DIGITAL INTEGRATOR

The digital integration of the signal output from the radiometer can be realized numerically in a computer that reads the data from the ADC.

If we were to solve the integrator as an analog one, it would be implemented as an RC low-pass filter. The relations between the noise bandwidth b, the equivalent integration time τ, given by the values of the passive RC elements and the cut-off frequency f_c are determined by the relation [4]:

$$b = \frac{1}{2\tau} = \frac{1}{4RC} = \frac{\pi}{2} f_c. \quad (15)$$

From the above-mentioned relationship, it is possible to calculate that with an integration time of 10 ms (used in actual radiometer), the equivalent bandwidth will be $b = 50$ Hz and the cut-off frequency $f_c = 31.83$ Hz. Even if the integrator will be implemented digitally, it is necessary to place an anti-aliasing filter in front of the ADC. This can be basically implemented as an analog filter (integrator) using an operational amplifier. However, this anti-aliasing filter affects the digital integrator, and for that reason it is necessary to reduce its integration time to approximately half the time of the digital integrator (5 ms for an integration time of 10 ms).

6 REALIZATION OF THE RADIOMETER OUTPUT CIRCUITRY

Due to the necessity of using an anti-aliasing filter at the output of the radiometer detector and its subsequent amplification, the output circuitry of the radiometer was designed and constructed.

The circuit shown in Fig. 4 uses the AD8599 ultra-low-noise operational amplifier, which contains two operational amplifiers (OAs) in one package.
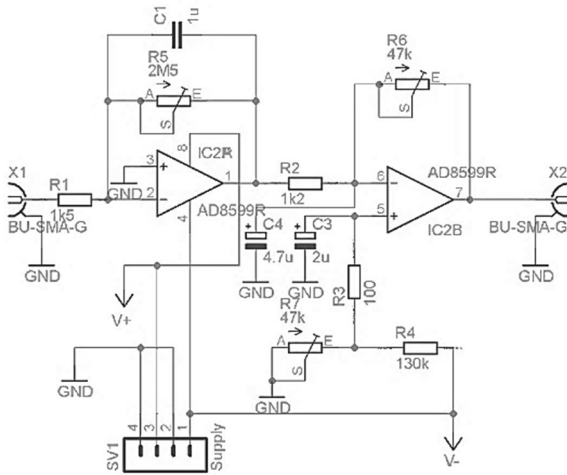
Fig. 4 Wiring diagram of radiometer output circuitry
Source: authors.

The first OA (IC2A) is wired as an integrator with an active element, and it is used as an antialiasing filter (first-order filter). The integration time is set by capacitor C1 and trimmer R5. The time constant is given by $\tau = C_1 R_5$, which corresponds to the corner angular frequency $\omega = 1/(C_1 R_5)$. With the specified parameters of the components, the maximum integration time is 2.5 seconds. The gain of this first stage is:

$$G_1 = \frac{R_5}{R_1}. \quad [-] \tag{16}$$

Frequency response of this antialiasing filter is in Fig. 5.
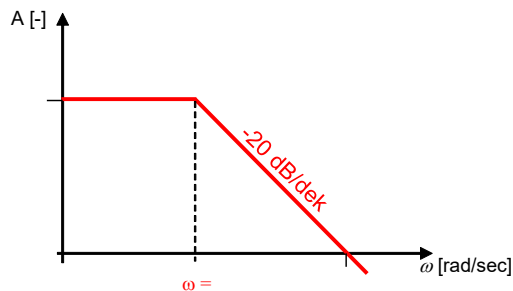
Fig. 5 Frequency response of antialiasing filter
Source: author.

The second OA (IC2B) represents a DC amplifier, where the gain of the amplifier is adjusted by the trimmer R6. The gain of the DC amplifier is:

$$G_2 = \frac{R_6}{R_2}. \quad [-] \tag{17}$$

Trimmer R7 serves to set the zero level at the output of the DC amplifier. The output of the DC amplifier is connected to an ADC. After A/D conversion, the signal is processed in the computer.

The Fig. 6 shows the prototype of the low-frequency circuitry.
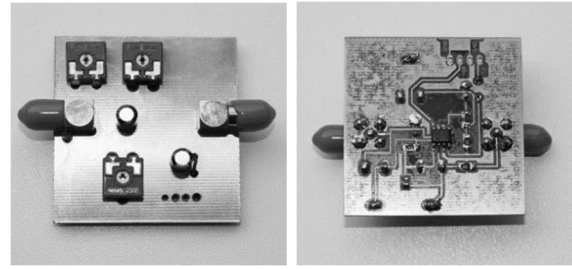
Fig. 6 Photography of top and bottom side of the low-frequency circuitry
Source: author.

7 RADIOMETER OUTPUT SAMPLING

The proposed radiometer is used to measure temperatures in the range of 0 K to 313 K with a sensitivity of about 0.05 K. It is unacceptable that we worsen these parameters by inappropriate digital processing.

For sampling, we will use an 8-channel, 16-bit AD converter (ADC) from National Instruments, type NI USB-6221. It allows measuring in the ranges ±1V, ±2V, ±5V and ±10V.

Sixteen bits allow the resolution of 1 to 65,536 quantization levels. To prevent overflow (exceeding the range of the ADC) we will use only 95% of the input range of the converter. It allows sampling with a resolution of $0.95 \cdot 65,536 = 62,295$ quantization levels.

To sample the temperature range of 313 K, we can achieve this with precision:

$$313 \text{ K} / 62,295 = 0.005 \text{ K}, \tag{18}$$

thus, due to sampling, the sensitivity of the radiometer will not deteriorate.

If we need to achieve an integration time of 10 ms, then we need to set the sampling rate of the ADC when capturing 1024 samples of the input signal:

$$f_s = \frac{1024}{\tau} = \frac{1024}{10 \times 10^{-3}} = 102,400 = 102.4 \text{ kHz}. \tag{19}$$

The used ADC allows to record with a sampling frequency f_s of a maximum of 250 kHz. We choose 100 kHz as the sampling frequency. It follows the minimum integration time will be:

$$\tau = \frac{1024}{f_s} = \frac{1024}{100 \times 10^3} = 10.24 \text{ ms}. \tag{20}$$

The direct detection radiometer sensitivity is like a total power radiometer sensitivity and is given by [4]:

$$\Delta T = \frac{T_{ref} + T_N}{\sqrt{B\tau}}, \tag{21}$$

where T_{ref} is a temperature of reference load (313 K), B is a radiometer front-end bandwidth (measured bandwidth is 11.7 GHz). T_N is overall noise temperature of radiometer front-end components and can be calculated by [6]:

$$T_N = 290(NF - 1) = 290(1.9526 - 1) =$$
$$= 276.254 \text{ K.}$$

$$(22)$$

where NF is a noise temperature of the radiometer front-end (its value is in Tab. 1.).

To understand above mentioned variables and their values see Fig. 3.

The resulting sensitivity of the radiometer according to (21) is:

$$\Delta T = \frac{313 + 276.254}{\sqrt{11.7 \times 10^9 \cdot 10.24 \times 10^{-3}}} = 0.0538 \text{ K.} \quad (23)$$

Even though integration time is set to 10 ms we can see the resulting sensitivity of the radiometer is very high.

8 CONCLUSION

In this article, we presented the design and construction of the output circuitry for the millimeter- wave radiometer.

The concept of this circuitry was based on calculations of the minimum and maximum value of the output voltage from the radiometer detector for temperatures from 0 K up to 313 K.

The output circuitry uses commercial ultra-low-noise operational amplifier AD8599 that contains two operational amplifiers in single package.

It was shown that the noise of this OA does not have a significant effect on the resolution of the radiometer used.

The presented circuitry is a perspective solution for millimeter-wave or microwave radiometers.

References

[1] QuinStar, *Product Application Notes – Millimeter-Wave Radiometers.* [cit. 2023-01-27]. Available at: https://quinstar.com/application-notes/application-notes-millimeter-wave-radiometers/

[2] ŠOSTRONEK, Mikuláš et al. W-band direct detection radiometer model. In *2015 International Conference on Applied Electronics* (AE). IEEE, 2015. p. 221-224.

[3] Farran Technology Ltd., *W-band Direct Detection Module With 2 x LNA, 1 x Filter, 1 x Detector*, Job No: 1942 Elsinco, datasheet, pp. 1-5, January 2007.

[4] LE VINE, David and SKOU, Neil. *Microwave radiometer systems: Design and analysis.* Artech, 2006.

[5] ŠOSTRONEK, Mikuláš. *Radiometry in millimeter band*. (in Slovak). Habilitation thesis. Liptovský Mikuláš: Armed Forces Academy of General M. R. Štefánik, 2019.

[6] RICHARDS, A. Mark, SCHEER, A. James and HOLM, A. William. 2010. *Principles of Modern Radar: Basic Principles*. Scitech Publishing, 2010, ISBN 978-1891121524. Available at: https://doi.org/10.1049/SBRA021E.

Assoc. Prof. Dipl. Eng. Mikuláš **ŠOSTRONEK**, PhD.
Armed Forces Academy of General M. R. Štefánik
Department of Electronics
Demänová 393
031 01 Liptovský Mikuláš
Slovak Republic
E-mail: mikulas.sostronek@aos.sk

Dipl. Eng. Miroslav **MATEJČEK**, PhD.
Armed Forces Academy of General M. R. Štefánik
Department of Electronics
Demänová 393
031 01 Liptovský Mikuláš
Slovak Republic
E-mail: miroslav.matejcek@aos.sk

Dipl. Eng. Zdeno **BARÁNI**, PhD.
Armed Forces Academy of General M. R. Štefánik
Department of Electronics
Demänová 393
031 01 Liptovský Mikuláš
Slovak Republic
E-mail: zdeno.barani@aos.sk

Mikuláš Šostronek was born in 1972 in Bojnice (Slovak Republic). He received his engineer degree in 1996 at Air Defense Faculty, Military Academy in Liptovský Mikuláš and PhD. degree in 2001 at Military Academy in Liptovský Mikuláš. He works as associated professor at Department of Electronics, Armed Forces Academy in Liptovský Mikuláš. His research area includes control systems and microwave engineering.

Miroslav Matejček was born in 1979 in Liptovský Mikuláš (Slovak Republic). He received his engineer degree in 2002 and PhD. degree in 2018, at Department of Air Defense, Military Academy in Liptovský Mikuláš. He works as an assistant professor at Armed Forces Academy in Liptovský Mikuláš. His research area includes guided weapon systems and control systems.

Zdeno Baráni was born in 1973 in Liptovský Mikuláš (Slovak Republic). He received his engineer degree in 1996 at Air Defense Faculty, Military Academy in Liptovský Mikuláš and PhD. Degree in 2005 at Armed Forces Academy in Liptovský Mikuláš. His research area applied electronics, image processing.

ZOOM OPTICAL SYSTEM FOR THERMAL CAMERA IN OPTICAL RANGE 8-14 μm

Chi Toan DANG, Vratislav KREHEĽ, Michal MOZOĽA

Abstract: Continuous infrared zoom systems with image quality and image stabilisation maintained throughout the workflow are increasingly being used. A long-wave infrared continuous zoom optical system with a 6x zoom ratio operating with an uncooled detector was designed. The optical system has a focal length from 37,5 mm to 225 mm, and the F/# is 1,5. The system includes 7 lenses with 3 even aspheres. The results show that the MTF function is very close to the diffraction limit curve over the entire focal range, proving that the system meets the specifications.

Keywords: Zoom optical system; Thermal infrared; Zoom ratio.

1 INTRODUCTION

The infrared zoom (IR) optical system is capable of detecting, tracking and continuously acquiring information, so with the development of the new generation of uncooled detectors, much more compact zoom thermal imaging devices were born [1, 2]. Because the IR zoom optical system has a continuously variable focal length, to ensure the image quality of the system in the entire focal range, image compensation must be calculated. The calculation of image compensation is usually based on two methods: optical compensation and mechanical compensation. According to the optical compensation method, the image plane can only be stabilised at a few different focal positions, so this method is suitable for designing optical systems with low zoom ratios. In contrast, the mechanical compensation method ensures that the optical system changes focus continuously over a certain range and is therefore widely used in high-ratio IR zoom optical systems. This paper refers to the design of a mechanically compensated IR-zoom optical system, using 7 lenses, with a high zoom ratio, which meets the research direction of versatile thermal imaging equipment.

2 CALCULATION OF A ZOOM IR OPTICAL STRUCTURE

From the general theory of the mechanically compensated IR zoom system [1, 2, 3, 4, 5], the principal diagram of the mechanically compensated zoom system is selected including the following four main groups shown in Fig.1:
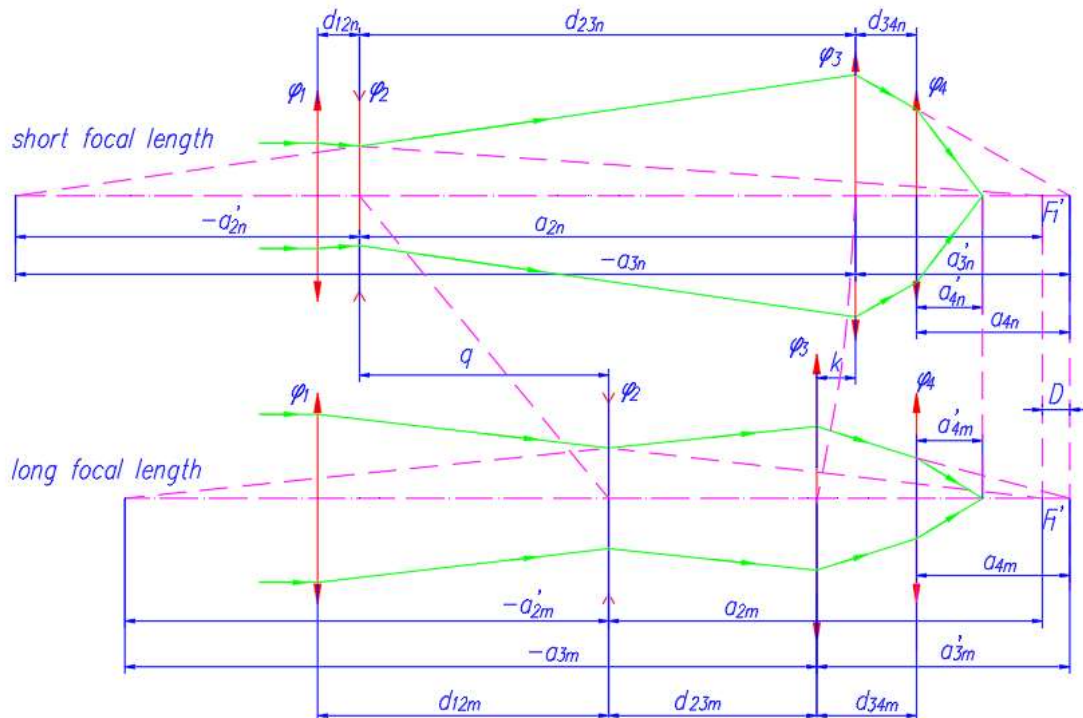

Fig. 1 Diagram of the principle of positive compensation in the IR zoom optical system
Source: authors.

In which, φ_1 is the **front fixed group**, φ_2 is the **variable/transform group**, φ_3 is the **compensatory/offset group**, and φ_4 is the **rear fixed group**. When the optical system is at the short focal position, the variable group φ_2 close to the front fixed group φ_1 and the positive compensation group φ_3 is near the rear fixed group φ_4. When the system moves to the long focal position, the variable group φ_2 shifts to the right and the compensatory group φ_3 shifts in the opposite direction, forming the shortest distance d_{23m} between the variable group and the compensatory group [2, 3].

To determine the initial structure of the system, Gaussian optical calculations are used, and the focal lengths of the displacement groups (variable group and offset group) f_2' and f_3' are respectively preselected. The structure of the optical system diagram is taken from the long focal position as a basis for the calculation. Horizontal magnifications at the long focal position of the shifting groups are β_{2m} and β_{3m} respectively.

The following expression can be established from the optical figure in the diagram in Figure 1:

$$d_{23m} = -a_{3m} - (-a_{2m}') = a_{2m}' - a_{3m}, \qquad (1)$$

in which d_{23m} is the shortest distance between the variable group and the compensatory group (at the long focal position); a_{2m}' is the distance of the image point built across/through the variable group; a_{3m} is the object point distance to the offset group.

The horizontal magnifications of the displacement groups are calculated as follows.

$$\beta_{2m} = \frac{f_2'}{a_{2m}+f_2'} = -\frac{a_{2m}'-f_2'}{f_2'}, \qquad (2)$$

$$\beta_{3m} = \frac{f_3'}{a_{3m}+f_3'} = -\frac{a_{3m}'-f_3'}{f_3'}. \qquad (3)$$

Transforming Equations (2) and (3) to get:

$$a_{2m}' = f_2'(1 - \beta_{2m}), \qquad (4)$$

$$a_{2m} = \frac{f_2'}{\beta_{2m}} - f_2', \qquad (5)$$

$$a_{3m} = \frac{f_3'}{\beta_{3m}} - f_3'. \qquad (6)$$

Substituting equations (4) and (6) into (1) to get the distance:

$$d_{23} = f_2'(1 - \beta_{2m}) + f_3'(1 - \frac{1}{\beta_{3m}}). \qquad (7)$$

Let us consider the optical system at the short focal position. According to optical construction, there are:

$$q = d_{12n} - d_{12m}, \qquad (8)$$

$$q + a_{2m} = a_{2n}, \qquad (9)$$

where q is the displacement of the group φ_2; d_{12n} is the distance between group φ_1 and group φ_2 in a short focal position; d_{12m} is the distance between group φ_1 and group φ_2 in a long focal position; a_{2n} is object distance to group φ_2 in a short focal position.

Using the formula in Eq. (2) for calculating the horizontal magnification of the variable group at the short focal position, we obtain:

$$a_{2n} = \frac{f_2'}{\beta_{2n}} - f_2' \qquad (10)$$

Substituting (5) and (10) into (9) and transforming to get:

$$\beta_{2n} = \frac{f_2' \cdot \beta_{2m}}{q \cdot \beta_{2m} + f_2'}. \qquad (11)$$

Equation (11) calculates the horizontal magnification of the point object through the variable group at the short focal position β_{2n} depending only on the amount of displacement q, the focal length f_2' and the horizontal magnification β_{2m} at the long focal position [2].

Find the magnification β_{3n} of the compensation group at the short focal position:

From the geometric relationship of the distance of object–image points through the zoom unit, it is easy to find the relationship between variable group magnification and offset group magnification when shifting from the long focal position to the short focal position (zoom equation) as follows [3].

$$f_3'\left(\frac{1}{\beta_{3m}} + \beta_{3m} - \frac{1}{\beta_{3n}} - \beta_{3n}\right) + f_2'\left(\frac{1}{\beta_{2m}} + \beta_{2m} - \frac{1}{\beta_{2n}} - \beta_{2n}\right) = 0. \qquad (12)$$

Transforming equation (12) to find β_{3n}:

$$\beta_{3n}^2 - b.\beta_{3n} + 1 = 0. \qquad (13)$$

where b is the coefficient that has the value:

$$b = -\frac{f_2'}{f_3'}\left(\frac{1}{\beta_{2n}} - \frac{1}{\beta_{2m}} + \beta_{2n} - \beta_{2m}\right) + \left(\frac{1}{\beta_{3m}} + \beta_{3m}\right). \qquad (14)$$

Solve the quadratic equation to find the value of β_{3n} according to the expression:

$$\beta_{3n} = \frac{b \pm \sqrt{b^2 - 4}}{2}. \qquad (15)$$

This expression shows that, during zooming, corresponding to one magnification of the transform group, there will be two magnifications of the compensating group that satisfy the requirement for image surface stability.

Calculate the amount of displacement k of the compensation group:

From the diagram in Figure *1*, it can be seen that the optical zoom objective system has a fixed image plane, which implies the following.

$$a'_{4n} = a'_{4m}. \qquad (16)$$

Therefore, their conjugate segments must be equal:

$$a_{4n} = a_{4m}. \qquad (17)$$

The amount of displacement k of the compensation group is equal to:

$$k = d_{34m} - d_{34n}. \qquad (18)$$

Combining (17) with (18) we have:

$$k = (d_{34m} + a_{4m}) - (d_{34n} + a_{4n}) = a'_{3m} - a'_{3n}. \qquad (19)$$

From the expression for calculating horizontal magnification according to Gaussian optics, the values of the image line segment built through the compensation group in the two configurations can be calculated as follows.

$$a'_{3m} = f'_3(1 - \beta_{3m}), \qquad (20)$$

$$a'_{3n} = f'_3(1 - \beta_{3n}). \qquad (21)$$

Substituting a'_{3m}, a'_{3n} from (20) and (21) into the expression (19) to get:

$$k = f'_3(\beta_{3n} - \beta_{3m}). \qquad (22)$$

The effective focal length of the optical system at the long focal position is

$$f'_m = f'_1 \cdot \beta_{2m} \cdot \beta_{3m} \cdot \beta_4, \qquad (23)$$

where β_4 is the horizontal magnification of the rear fixed lens group. Due to the requirement that the image plane does not change, β_4 remains constant during the zooming process of the zoom objective system.

The general focal length of the optical system at the short focal position is:

$$f'_n = f'_1 \cdot \beta_{2n} \cdot \beta_{3n} \cdot \beta_4. \qquad (24)$$

The zoom ratio is formed by the variable focal length of the zoom objective and is defined as Γ:

$$\Gamma = \frac{f'_m}{f'_n}. \qquad (25)$$

Combining (23), (24), and (25) we have the following relationship of the product of magnifications of mobile components in two polar configurations:

$$\Gamma = \frac{\beta_{2m} \cdot \beta_{3m}}{\beta_{2n} \cdot \beta_{3n}}. \qquad (26)$$

Equation (26) shows the relationship of the zoom ratio of the objective zoom optical system Γ to the product of the horizontal magnifications of the moving components in the two extreme configurations.

The distance between the variable group and the offset group at the short focal position is (see Figure 1):

$$d_{23n} = q + d_{23} + k. \qquad (27)$$

Calculate the focal length f'_1 according to the formula:

$$f'_1 = d_{12n} + a_{2n}. \qquad (28)$$

Replace a_{2n} in Equation (10) into Equation (28) to get:

$$f'_1 = d_{12n} + f'_2 \left(\frac{1}{\beta_{2n}} - 1 \right). \qquad (29)$$

Calculating the total length of the objective optical system: If the length of the objective optical system L is considered as the distance from the position of the fixed lens group in advance to the position of the image plane, then L can be calculated by the expression:

$$L = d_{12n} + q + d_{23m} + k + d_{34n} + a'_{4n}. \qquad (30)$$

From the formulas built above, the initial structure of the optical system can be found [1, 2, 3].

3 DESIGN OF THE IR ZOOM SYSTEM

3.1 Feature criteria of the optical zoom system to be designed

Choosing a set of design criteria for the IR zoom optical system based on the working distance of the equipment calculated according to Johnson's standard, combined with the selection of Flir's 640 x512 uncooled detector, which is commercially available, is valued as in Table *1*.

From the set of indicators, it is necessary to design and allocate the component focal lengths and the distance between the components (groups) of the zoom objective to obtain the zoom ratio and maintain the overall length of the optical system. At the same time, no collision of the components occurs when moving.

Tab. 1 The set of criteria and features of the optical zoom system to be designed

No.	Parameter	Value
1	Detector, pixel	640 x 512
2	The pitch of the detector pixels, μm	17
3	Working wavelength range, μm	8 ~ 12
4	Working focal range, *mm*	37,5~225
5	F/#	1,5
6	Zoom ratio, *times*	6
7	Lens length L, mm	≤ 300

Source: authors.

3.2 Design results

The distribution of this IR zoom system is: +, '-', '+', and '+' in which the mobile group '-' performs zooming, and the movable group '+' performs image plane offset compensation. The movement of these two moving groups is ensured by a special cam mechanism.

To perform the optical system calculations, formulas from (*1*) to (*30*) are used. The optical materials Ge and ZnS, which are common and easy to machine and have different refractive indices and Abbe coefficients, are chosen. They help to eliminate axial chromatic aberration. The structure of the system at *six* different focal positions is shown in Figure *2*.

a) $f' = 225$mm. b) $f' = 180$mm. c) $f' = 135$mm.

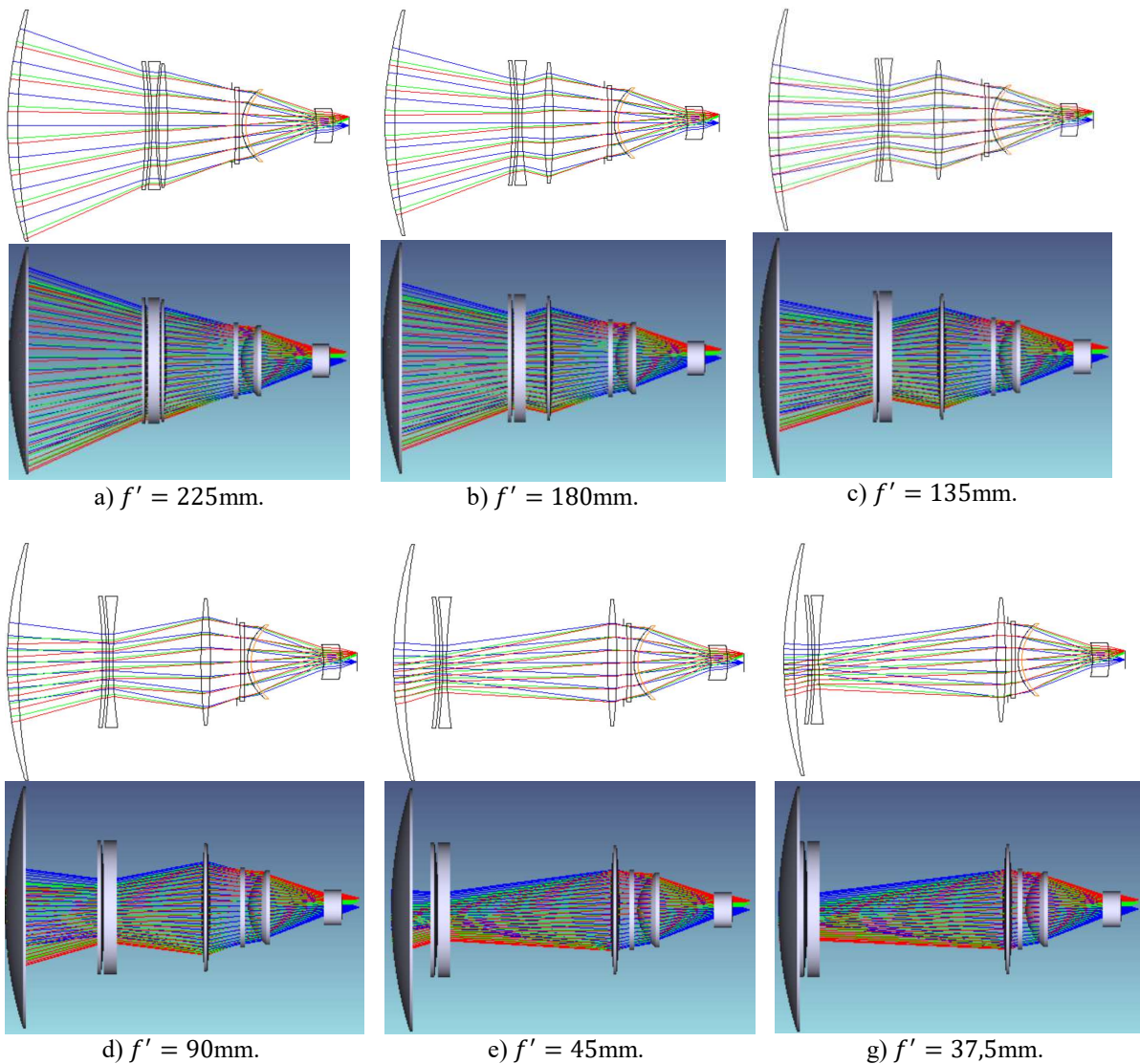d) $f' = 90$mm. e) $f' = 45$mm. g) $f' = 37,5$mm.

Fig. 2 Structure of the IR zoom optical system
Source: authors.

The optical system consists of 7 lenses, of which 6 are made of Ge and 1 is made of ZnS. The fixed group φ_1 is a single lens made of Ge, the variable group φ_2, which has negative power, consists of two lenses that perform the zoom, the third group φ_3 is a positive lens that compensates for the image plane shift. The most complex rear fixation group φ_4 consists of 3 lenses to eliminate residual aberrations from the front groups. The system has *3* even aspherical surfaces to eliminate higher-order aberrations. Applying the multi-configuration optimization in Zemax [6], the structure of the IR-zoom optical system is given in Table *2* with the multi-configuration variable being the distances between groups $\varphi_1, \varphi_2, \varphi_3, \varphi_4$. During the design process, the sum of these three distances is constant and equal to *151,32* mm; the image plane is kept stable. The total length of the system is *265* mm and the constant F# is *1,5*.

Table 3 shows the Lens Data Editor of Configuration *1* (f'=225 mm), in which the optical surfaces numbered *2, 10,* and *14* are even aspheres to reduce aberrations. The system Stop on the ninth surface with a semi-diameter of *27,97 mm* is unchanged.

Tab. 2 Multi-configuration variable of the IR zoom optical system

Active : 3/6		Config 1	Config 2		Config 3*		Config 4		Config 5		Config 6	
1: APER	0	1.500	1.500	P	1.500	P	1.500	P	1.500	P	1.500	P
2: YFIE	2	4.930	4.930	P	4.930	P	4.930	P	4.930	P	4.930	P
3: YFIE	3	7.000	7.000	P	7.000	P	7.000	P	7.000	P	7.000	P
4: THIC	2	99.072 V	92.885	V	81.746	V	64.205	V	24.187	V	11.077	V
5: THIC	6	2.000 V	17.620	V	37.556	V	66.644	V	121.788	V	138.100	V
6: THIC	8	50.250 V	40.818	V	32.021	V	20.474	V	5.348	V	2.146	V

Source: authors.

Tab. 3 The Lens Data Editor of Configuration 1 (f'=225 mm)

Lens Data Editor: Config 1/6

Surf:Type		Radius		Thickness		Glass		Semi-Diameter	
OBJ	Standard	Infinity		Infinity				Infinity	
1*	Standard	302.396	V	7.989	V	GERMANIUM		90.000	U
2*	Even Asph..	525.492	V	99.072	V			90.000	U
3*	Standard	-440.871	V	3.000	V	GERMANIUM		50.000	U
4*	Standard	-397.279	V	2.051	V			50.000	U
5*	Standard	-397.279	P	3.000	V	GERMANIUM		50.000	U
6*	Standard	352.714	V	2.000	V			50.000	U
7*	Standard	419.533	V	7.057	V	GERMANIUM		48.000	U
8*	Standard	-469.091	V	50.250	V			48.000	U
STO	Standard	Infinity		2.581	V			27.972	
10*	Even Asph..	-756.110	V	3.000	V	GERMANIUM		30.000	U
11*	Standard	-3320.665	V	2.000	V			30.000	U
12*	Standard	35.746	V	3.001	V	GERMANIUM		28.000	U
13*	Standard	36.102	V	54.846	V			28.000	U
14*	Even Asph..	-86.108	V	12.926	V	ZNS_BROAD		13.000	U
15*	Standard	-73.990	V	12.227	V			13.000	U
IMA	Standard	Infinity		–				7.046	

Source: authors.

3.3 Evaluate image quality

MTF is one of the criteria to evaluate the quality of the optical system image designed. The MTF functions of the system in different focal configurations are shown in Figures *3(a)* to *(g)*. The curves have a cutoff frequency of *30* lines/mm, with values above *0,25* and close to the diffraction limit, showing that the quality of the design system is acceptable [7].

a) $f' = 225$mm   b) $f' = 180$mm   c) $f' = 135$mm

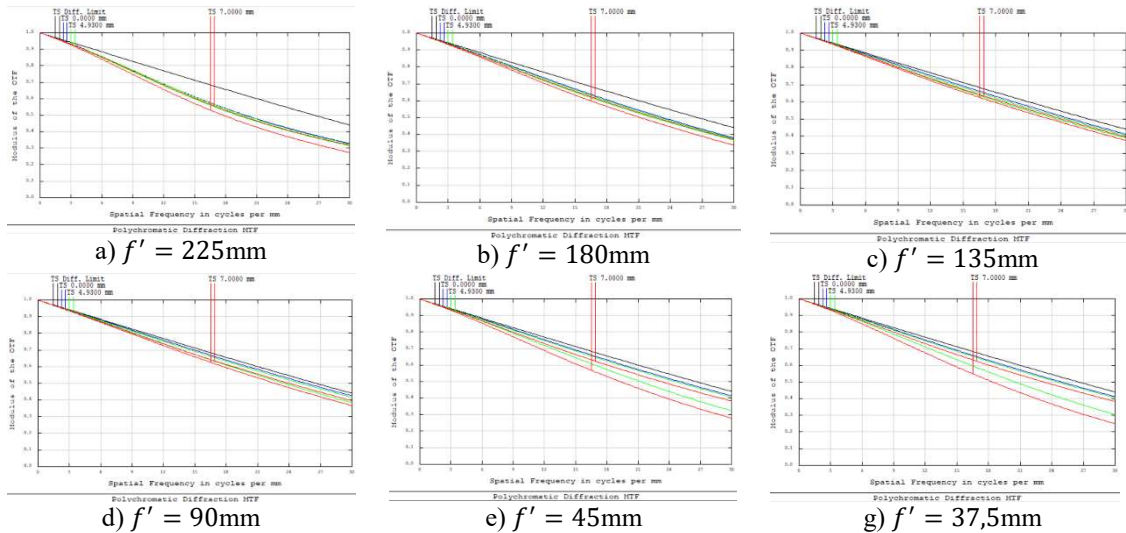d) $f' = 90$mm   e) $f' = 45$mm   g) $f' = 37,5$mm

Fig. 3 MTF curve of the optical zoom system at different focal lengths
Source: authors.

The spot diagram in the image plane of the optical system is also an indicator of quality. Figure *4* shows the spot diagram of *6* different focal positions of the designed zoom optical system. In Figure *4*, it can be seen that the RMS ray spot size at all positions is smaller than the pixel size, so the zoom system satisfies the image quality requirements of the detector.
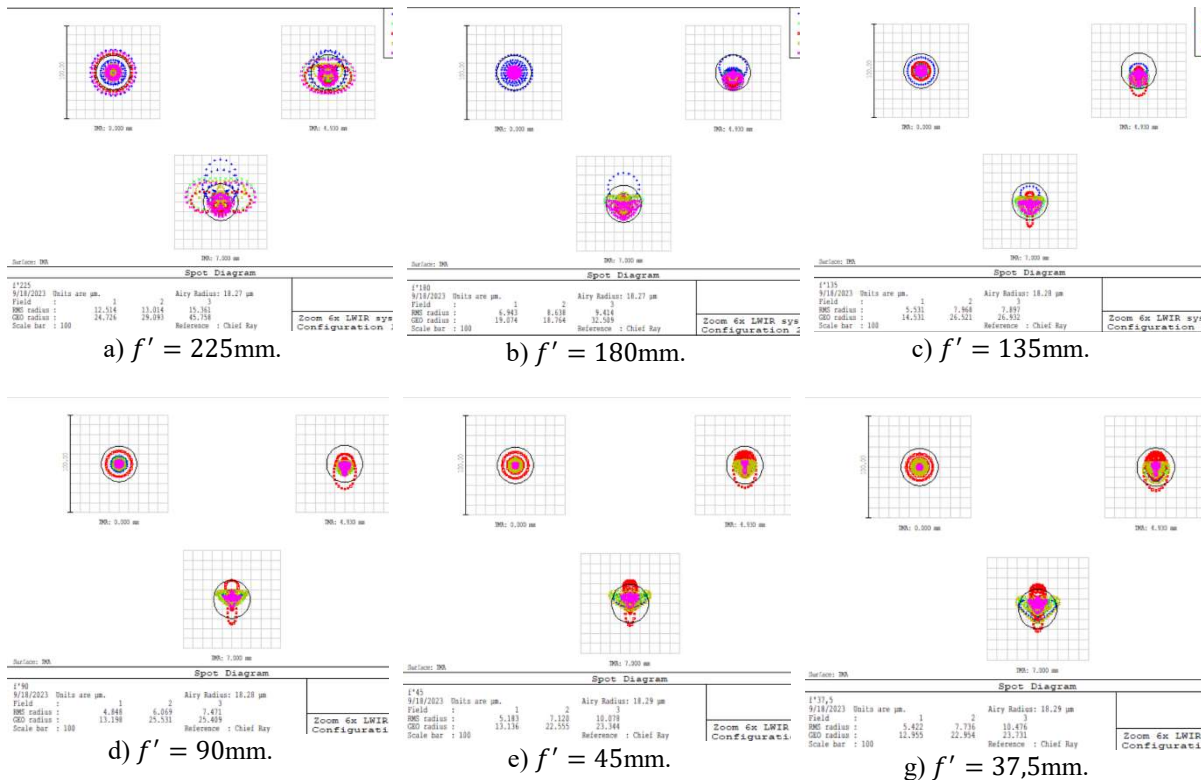

a) $f' = 225$mm.   b) $f' = 180$mm.   c) $f' = 135$mm.

d) $f' = 90$mm.   e) $f' = 45$mm.   g) $f' = 37,5$mm.

Fig. 4 Spot diagram at different focal positions
Source: authors.

4 CONCLUSION

An IR continuous-zoom optical system was designed in the LWIR range with a 6x zoom ratio operating with a 640x512 pixel uncooled detector. Evaluating the quality of the MTF function and the spot diagrams shows that the zoom system is quite good quality. Zoom optical system with continuously variable focal length from *37,5* mm to *225* mm, constant F/#*1.5*, compact structure, suitable for target positioning and search applications in the LWIR waveband.

The design of the infrared zoom optical system needs to continue in the direction of uniformly increasing image quality throughout the entire zoom range, paying attention to the feasibility of the motion curve of the compensation cam mechanism and further expanding the zoom ratio, meeting the increasing requirements for observing and tracking thermal targets.

References

[1] MU Da, DU Yu-nan, Mi Shi-long and GUO Yan-chi. *Design of 10x uncooled thermal infrared zoom optical system,* Proc. of SPIE Vol. 8907.

[2] YAN Jing, SUN Quan, LIU Ying, ZHOU Hao, HUAN Ke-wei, SHI Xiao-guang. *High ratio long-way infrared continuous zoom system*, Proc. of SPIE Vol. 8907.

[3] Tao ChunKan. *Varifocal differential equation theory of zoom lens*. 168/SPIE Vol.2539.

[4] AD Clark. *Zoom lenses.* Adam Hilger, 1973.

[5] Allen Mann. *Infrared optics and zoom lenses. Volume TT83*, 2009. Available at: https://doi.org/10.1117/3.829008.

[6] Zemax 13 Premium Programme. 2014.

[7] Available at: https://www.ophiropt.com/infrared/

Chi Toan **DANG**
University of Defence
Kounicova 65
662 10 Brno
Czech Republic
E-mail: chitoan.dang@unob.cz

Dipl. Eng. Vratislav **KREHEĽ**
Armed Forces Academy of General M. R. Štefánik
Demänová 393
031 01 Liptovský Mikuláš
Slovak Republic
E-mail: vratislav.krehel@aos.sk

Capt. Dipl. Eng. Michal **MOZOĽA**
Armed Forces Academy of General M. R. Štefánik
Demänová 393
031 01 Liptovský Mikuláš
Slovak Republic
E-mail: michal.mozola@aos.sk

Chi Toan DANG was born in 1978. He graduated from Le Qui Don University of Technology, Hanoi, Vietnam in 2002 as an optical instrument engineer. He graduated with a Master's degree from Le Qui Don Technical University, Hanoi, Vietnam in 2018, majoring in optoelectronics. He worked in the optoelectronics factory, under the General Department of Defence Industry of Vietnam (2002-2011). Then he worked at the Weapons Institute of Vietnam, General Department of Defence Industry of Vietnam (since 2011). Currently, he is working as a doctoral student at the University of Defence, Brno, Czech Republic. Participated in optical processing technology, total installation of night vision devices, measurement, design of night vision lenses, and infrared lenses.

Vratislav KREHEĽ was born in Liptovský Mikuláš, Slovakia in 1972. He received his M. Sc (Eng.) at the Military Academy in Liptovský Mikuláš in 2003. He started his dissertation studies in 2021. His research interests are focused on optimization of sniper weapons fire mode. He is currently working as an assistant professor at the Department of Mechanical Engineering, Armed Forces Academy of General M. R. Štefánik in Liptovský Mikuláš.

Michal MOZOĽA was born in Krupina, Slovakia in 1988. He received his M. Sc (Eng.) at the Armed Forces Academy in Liptovský Mikuláš in 2017. He started his dissertation studies in 2022. His research interests are focused on the optimisation of automatic weapon fire modes. He is currently working as an assistant professor at the Department of Mechanical Engineering, Armed Forces Academy of General M. R. Štefánik in Liptovský Mikuláš.

SCIENCE & MILITARY - WRITER´S GUIDELINES

1. Scientific articles submitted for publishing have to be original, topical and never been published before.

2. Articles have to be written in English language and in accordance with ethical standards. For more details, please visit the website of the Science & Military Journal (http://sm.aos.sk/index.php/en/for--authors-en/ethical-standards).

3. Length of the article should not exceed 6 pages in defined format. Microsoft Word text editor must be used for writing. Articles must be written using Times New Roman, single line spacing and follow the following form: Title -12 point bold capital letters aligned to the center. Full author´s (co-author´s) name – 10 point normal letters aligned to the center. Abstract – 9 point normal letters, extent 3-5 lines. Keywords – 9 point normal letters. The article text – 10 point normal letters. Contact - full author´s (co-author´s) name, affiliation, e-mail – 9 point normal letters at the end of the article. The article text will be written in 2 columns format with a 75 mm column width and 10 mm empty space separating the columns. The first line of each paragraph must be shifted 5 mm to the right.

4. Upper and lower margins must be set to 25 mm, left and right margins to 20 mm. Select mirror margins and set binding margins to 10 mm. The distance between the header/footer and the page margin must be 12,5 mm, while different odd and even pages must be selected.

5. Photographs for publication must be in black-white (not in color) of excelent quality with good contrast.

6. Equations in the text are also to be written using the equation editor. (Equation must be typed in Microsoft Equation, which is an integral part of Microsoft text editor.) They must be numbered. Numbers are to be enclosed in parentheses and aligned to the right margin of a column.

7. Figures, graphs and tables must be included in the text and numbered and must contain description. Figures must be identified as Fig. 1 followed gradually by the figure description. Graphs must be identified as Graph 1 followed by the graph description. Tables must be identified as Tab. 1, followed by the table description.

8. References must be fully and accurately documented (according to ISO 690). References should be quoted in the text in square brackets and listed in the order they have appear in the text.

9. The specimen article that can be found on the web-site: http://sm.aos.sk/index.php/en/for-authors-en can be used as an example of the correct format.

10. The editorial board will consider submitted articles in the next scheduled meeting. If it decides to include the article in the next issue it submits the manuscript to the editors for the peer review. The final version (before printing) will be sent to the author for the final revision. The authors are fully responsible for the level of language.

11. Contributions in A4 format edited according to the specimen article should be submitted in one hard copy and also in electronic form to the Editorial board.

12. The deadlines for the delivery of the articles in calendar year are: March 1 and September 1.

Science & military

Content